LUND UNIVERSITY

Preclinical Molecular Imaging using Multi-Isotope Digital Autoradiography - Techniques and Applications

Örbom, Anders

2013

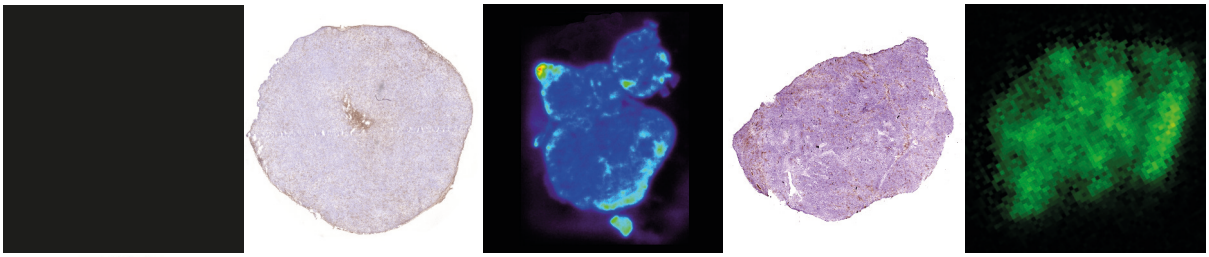

Preclinical Molecular Imaging using Multi-Isotope Digital Autoradiography

Techniques and Applications

ANDERS ÖRBOM
DEPARTMENT OF MEDICAL RADIATION PHYSICS | LUND UNIVERSITY

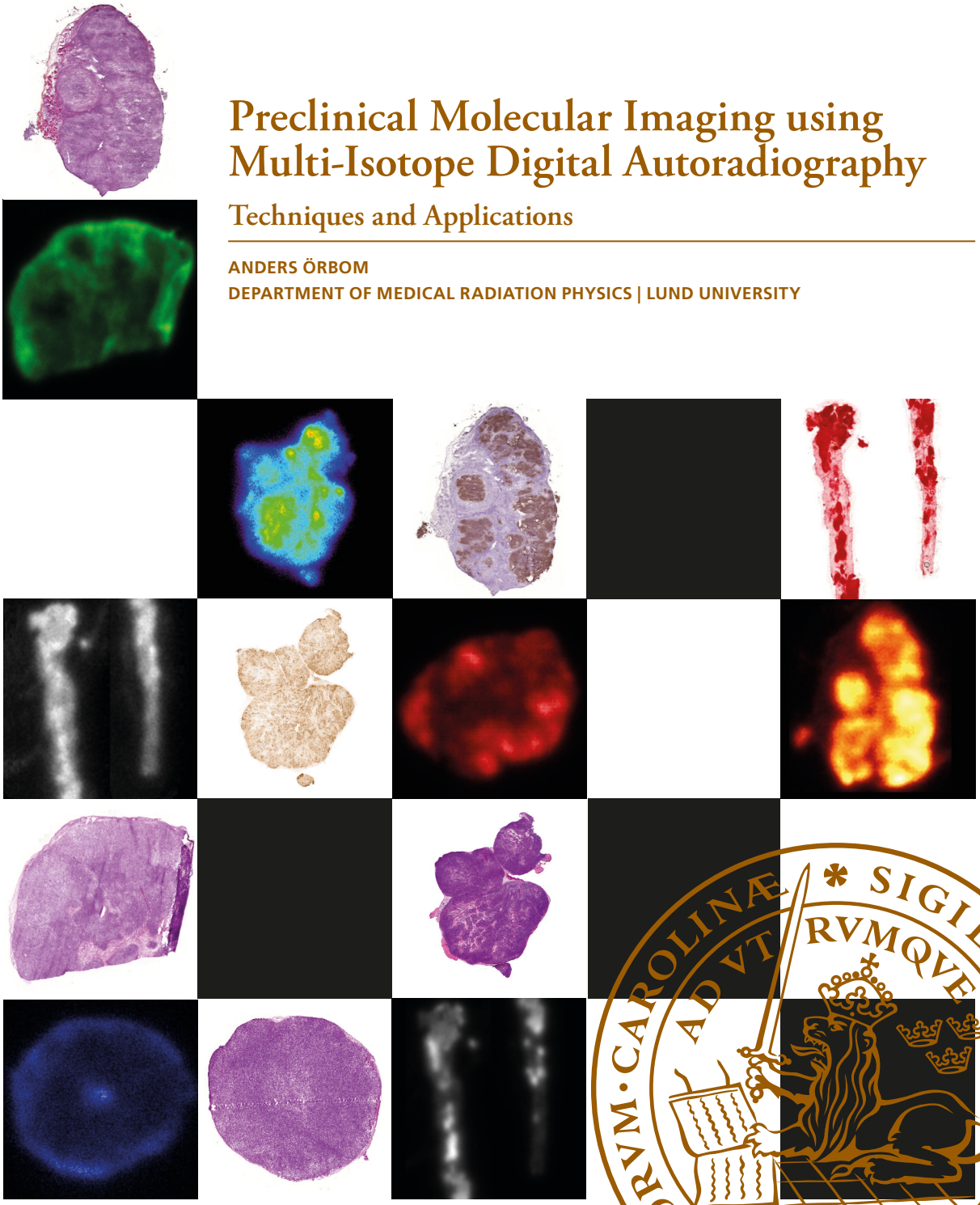

Preclinical Molecular Imaging using Multi-Isotope Digital Autoradiography

Techniques and Applications

Anders Örbom

LUND
UNIVERSITY

Department of Medical Radiation Physics,
Lund University, Sweden

Department of Medical Radiation Physics
Faculty of Science, Lund University

ISBN 978-91-7473-777-6 (print)
ISBN 978-91-7473-778-3 (pdf)

Printed in Sweden by Media-Tryck, Lund University
Lund 2013

The front cover illustration consists of various digital autoradiography images and stained tissue sections from the studies described in this thesis. The back cover illustration is a digital autoradiography image of an array of pieces of thin nickel wire, irradiated in a research reactor to contain the radioactive isotope Cobolt-58.

The spontaneity of the radiation is an enigma,
a subject of profound astonishment.

– Marie and Pierre Curie,
Report to the International
Congress of Physics, Paris, 1900

Abstract

Molecular imaging, both *in vivo* and *ex vivo*, is playing an increasingly important role in preclinical medical research. When using radionuclide-labeled tracers, e.g. in the development of radiopharmaceuticals for diagnostic imaging or for radionuclide therapy, quantitative *in vivo* imaging can be performed using emission tomography. Quantitative autoradiography of thin tissue sections is employed to obtain high-resolution images of the radioactivity distribution *ex vivo*, commonly using photographic film or a storage phosphor screen.

The aim of the work presented in this thesis was to evaluate the potential of digital autoradiography with multi-radionuclide imaging capabilities to contribute to preclinical, small-animal, research studies using radiolabeled targeting molecules for diagnosis or therapy.

The characteristics of a digital autoradiography system employing a double-sided silicon strip detector were investigated with regard to spatial resolution, detection sensitivity, background and noise, system dead time, and the ability to resolve energy spectra. This system, although it has a smaller field of view, was found to perform favorably compared to a storage phosphor system. Methods of separating the contributions from several radionuclides imaged simultaneously were developed and evaluated.

The intratumoral distribution of ^{177}Lu-labeled monoclonal antibodies (mAbs) over time was studied in a syngeneic rat model of colon carcinoma at both therapeutic and lower activity levels. The activity was initially found in the tumor periphery, then in areas of viable, antigen-expressing cells, and at 24-48 h and later in areas of granulation tissue and low antigen expression. A point-dose kernel was used to calculate the absorbed-dose rate distribution in tumor sections, which was found to be twice the section mean in areas with high activity accumulation.

The distributions of ^{111}In- and ^{177}Lu-labeled mAbs targeting intercellular adhesion molecule 1 were studied in a xenograft model of human prostate cancer, and compared with a control mAb as well as clinically used ^{18}F-labelled tracers using small animal SPECT/CT and PET/CT, as well as multi-radionuclide digital autoradiography. Results from this study, and those from an ^{125}I-labelled mAb compared with a co-injected smaller antibody fragment labeled with ^{131}I, both targeting carcino-embryonic antigen, confirmed that barriers to tumor penetration by macromolecules are a major problem, especially in radioimmunotherapy. A mAb against free prostate-specific antigen was also studied.

Using multi-radionuclide digital autoradiography, the plaque-to-aorta contrast of a mAb targeting oxidized low-density lipoprotein was observed to be higher than that of ^{18}FDG in slide mounted aortas from atherosclerotic mice.

These studies show that digital autoradiography, including multi-radionuclide imaging, has the potential to provide novel data for preclinical imaging studies, but that further development and optimization of the method are needed.

Keywords: Autoradiography, Radioimmunotherapy, Antibodies, Molecular Imaging, Multi-Radionuclide Imaging, Silicon-strip detector

Populärvetenskaplig sammanfattning

Bildgivande system har en allt mer framträdande roll inom sjukvård och medicinsk forskning. En del av dessa system fungerar genom att en patient eller ett försöksdjur injiceras med ett läkemedel märkt med ett radioaktivt ämne, och sedan mäts den strålning som detta ämne avger för att skapa en bild av var ämnet, och därmed läkemedlet, befinner sig. Det finns både system som mäter fördelningen av radioaktivitet i tre dimensioner hos levande individer (till exempel PET- eller SPECT-kameror) och sådana som mäter fördelningen på en mer detaljerad nivå i tunna vävnadssnitt som är tagna från avlivade försöksdjur; den senare metoden kallas för *autoradiografi*.

Den idag mest använda tekniken för autoradiografi baseras på plattor med fosfor-kristaller som fungerar ungefär som en svart-vit fotografisk film. De exponeras under en viss tid för vävnadsprovet med det radioaktiva ämnet, och sedan framkallas bilden med hjälp av en speciell utrustning. Det nya system som utvärderas och används i den här avhandlingen är istället en kiselbaserad halvledardetektor, och fungerar lite som en digital färgvideokamera jämfört med fosforplattorna. Det kan se signalerna från det radioaktiva preparatet i realtid, mäta när i tiden strålningen avges och vilken ”färg”, d.v.s. energi, den har.

Detektorsystemet testades och olika egenskaper mättes. Det visade sig ha en låg bakgrundssignal, god förmåga att för många, men inte alla, radioaktiva ämnen avgöra vilka energier som mättes, samt korrekt kunna mäta relativt starkt radioaktiva prov. Detaljnivån, d.v.s. upplösningen, i bilden jämfördes med fosforplattorna genom att en mycket tunn radioaktiv tråd avbildades på båda systemen. Kiseldetektorn hade en högre upplösning än fosforsystemet även om skillnaden inte var drastisk.

Systemet applicerades i en rad djurmodellstudier med antikroppar märkta med radioaktiva ämnen som känner igen vissa strukturer på celler i till exempel cancertumörer eller åderförkalkningsplack. Det observerades att i en råttmodell av koloncancer tar sig antikropparna först in i och behandlar tumören med strålning, men efter något dygn finns radioaktiviteten i områden av ärrvävnad i tumören där den kanske inte gör så stor nytta. Andra antikroppar testades i musmodeller av prostatacancer där de visade sig visserligen hitta tumören, men på grund av tumörens struktur och att antikroppar är relativt stora m.m. ofta ha väldigt svårt att nå in till tumörens inre. I en del av dessa studier användes flera antikroppar eller andra molekyler samtidigt och de märktes då med olika radioaktiva ämnen, som i bilden kunde separeras genom deras olika energi, eller hur snabbt de avger sin strålning. Ett sådant exempel var när en antikropp specifik mot åderförkalkningsplack testades samtidigt med en ospecifik antikropp och ett sockerliknande ämne som ackumuleras vid inflammation. Där kunde vi i en jämförelse se att den specifika antikroppen togs upp mer i plack än i omkringliggande kärlvägg. Detta i högre grad än det sockerliknande ämnet, men liknande den ospecifika antikroppen.

Sammantaget visade studierna att autoradiografi med ett modernt instrument som kan separera signalen från olika radioaktiva ämnen har mycket att tillföra i studier där man tar fram nya läkemedel eller diagnostiska preparat, men att teknik och metod fortfarande behöver utvecklas.

List of radionuclides

Selected characteristics of a selection of the radionuclides employed in this work or discussed in this thesis. All figures from the Brookhaven web database of nuclear decay data in the MIRD Format [1], based on source data from the International Network of Nuclear Structure and Decay Data.

		Selected radiations		
Radionuclide	**Half-life**	**Type**	**Yield (%)**	**Avg. energy (keV)**
^{18}F	109.8 min	β+	96.7	249.8
^{99m}Tc	6.007 hours	γ	89.0	140.5
		ce	8.79	119.5
^{211}At	7.214 hours	α	41.8	5870
		X-ray	21.1	79.29
^{90}Y	64.00 hours	β-	100	933.7
^{111}In	67.32 hours	γ	90.6	171.3
		γ	94.1	245.4
		ce	7.87	144.6
^{89}Zr	78.41 hours	β+	22.7	395.5
^{177}Lu	6.647 days	β-	79.4	149.4
		γ	10.4	208.4
^{131}I	8.025 days	β-	89.6	191.6
		γ	81.5	364.5
^{125}I	59.40 days	X-ray	73.5	27.47
		X-ray	39.4	27.20
		ce	10.7	30.55

Conversion electron emissions denoted by *ce*.

Acknowledgements

Many people have helped me in my work over the years, but I would especially like to thank the following.

My advisor, *Sven-Erik Strand*, who has guided and encouraged me all the way from my MSc project in Los Angeles to my doctorate. He has helped me keep my perspective among the day-to-day challenges of research. And for any imaginable problem I encountered, Sven-Erik somehow always knew just the right person to talk to. It has been a privilege to work with you.

Sophie Eriksson at the Department of Oncology, my co-author and collaborator on Papers II and III, and on rigorous scientific studies of pastries, cookies and cakes. Thank you for your excellent scientific work and the discussions that helped me to better understand biology, and for generally having all your ducks (or is that rats?) in a row.

Susan Evans-Axelsson, at the Division of Urological Cancers, my collaborator and co-author on Papers IV-VI, whose skill and insight took these studies from the drawing board to finished manuscripts. Special thanks for being my travel-buddy after WMIC 2010, and for accompanying me to weird temples/art museums in the Japanese mountains. Thanks also to her advisor, *Anders Bjartell*, for his valuable input.

Bo Jansson, at BioInvent International AB for nor only being an inexhaustible source of exciting ideas for new projects, as well as the antibodies needed to carry them out, but also for assistance with antibody labeling, manuscripts, and for occasionally transporting graduate students and materials back and forth between Lund, Malmö and Copenhagen.

Erika Elgström, who led the study described in Paper III, *Rune Nilsson* and *Jan Tennvall*, from the Radioimmunotherapy Group, for fruitful scientific exchanges that I hope will continue.

Bo Holmqvist, for being my co-advisor for a period and for, together with *Anna Ebbesson*, introducing me to histology and immunohistochemistry.

Anna Wu and *Tove Olafsen*, at the Department of Molecular and Medical Pharmacology at the University of California in Los Angeles, for making their resources and time available to me on many occasions, so that I could produce some of the initial multi-radionuclide images. Thanks also to *Magnus Dahlbom,* for his invaluable

assistance and advice on programming and image analysis during the work on my MSc project and later, and *Elena Heckathorne* and *Nicole Detorie*, for great company in the grad student bunker.

Håvard Hauge and the rest of the team at Biomolex AS in Oslo, for always responding to my questions, and for help in trouble-shooting and improving the digital autoradiography system.

Staff and researchers at the Department of Medical Radiation Physics, especially *Erik Larsson*, for his simulation of the point-dose kernel for Paper II, and *Katarina Sjögreen Gleisner*, for valuable advice on image analysis over the years.

The staff at the Lund Bioimaging Center, especially *Thuy Tran*, for valuable collaboration, help with labeling, and advice, and *Gustav Grafström*, for his help with the *in vivo* imaging instruments.

My many fellow PhD students at the Department of Medical Radiation Physics in Lund, including *Jonas Ahlstedt*, for his contributions to Paper I, and for being an amicable lab-mate and collaborator; *Renata Madru*, for sharing an office with me and for being a great, camera-tripod-wielding, traveling companion; *Mikael Pettersson* and *Jonathan Siikanen*, for collaboration on a couple of projects and for good talks on graduate student life. Thanks also to *Oskar Vilhelmsson Timmerman*, for his help with radiolabeling and more.

Pavel Golubev and *Bo Jacobsson* at the Department of Nuclear Physics, for collaboration on the 2-detector project not covered in this thesis.

My fellow autoradiographer *Tom Bäck* of α-camera fame at Gothenburg University, for some small but interesting joint projects. I hope we have the opportunity to work together more in the future.

Jan Nilsson, Gunilla Nordin Fredrikson and others at the Experimental Cardiovascular Research Unit, for helping me navigate the biology of atherosclerosis.

Henrik Hussein El Ali and *Anne Mette Fisker Hag* at the Panum Institute in Copenhagen, for their help with my first small-animal PET imaging.

Helen Sheppard, for language review of this thesis as well as Papers II-III.

My friends and my parents, for their unwavering support, especially when I was struggling with the logistics of my studies and when unclear data were getting me down.

This research was supported by grants from the Swedish Research Council, the Swedish Cancer Society, Mrs. Berta Kamprad's Foundation, Gunnar Nilsson's Foundation, Governmental Funding of Clinical Research within the National Health Service, and the Eurostars Programme through the Swedish Governmental Agency for Innovation Systems (VINNOVA).

Contents

List of original papers

I. Characterization of a Double-sided Silicon Strip Detector Autoradiography System.
Anders Örbom, Jonas Ahlstedt, Tom Serén, Iiro Auterinen, Petri Kotiluoto, Håvard Hauge, Karl Östlund, Tove Olafsen, Anna M. Wu, Magnus Dahlbom and Sven-Erik Strand
Manuscript

II. The intratumoral distribution of radiolabeled 177Lu-BR96 monoclonal antibodies changes in relation to tumor histology over time in a syngeneic rat colon carcinoma model
Anders Örbom*, Sophie E. Eriksson*, Erika Elgström, Tomas Ohlsson, Rune Nilsson, Jan Tennvall and Sven-Erik Strand
Journal of Nuclear Medicine, 2013, 54.8: 1404-1410.

III. Change in cell death markers during 177Lu-MAb radioimmunotherapy induced rejection of syngeneic rat colon carcinoma
Erika Elgström, Otto Ljungberg, Sophie E. Eriksson, **Anders Örbom**, Sven-Erik Strand, Tomas G. Ohlsson, Rune Nilsson, and Jan Tennvall
Manuscript

IV. Intratumoral distribution and pharmacokinetics of the radiolabeled ICAM-1 targeting monoclonal antibody R6.5 in a prostate cancer mouse model
Anders Örbom*, Susan Evans Axelsson*, Bo Jansson, Oskar Vilhelmsson Timmermand, Thuy A. Tran, Anders Bjartell, and Sven-Erik Strand
Manuscript

V. Targeting free prostate-specific antigen for in vivo imaging of prostate cancer using a monoclonal antibody specific for unique epitopes accessible on free prostate-specific antigen alone
Susan Evans-Axelsson, David Ulmert, **Anders Örbom**, Pernilla Peterson, Olle Nilsson, Johan Wennerberg, Joanna Strand, Karin Wingårdh, Tomas Olsson, Zandra Hagman, Vladimir Tolmachev, Anders Bjartell, Hans Lilja, and Sven-Erik Strand
Cancer Biotherapy and Radiopharmaceuticals, 2012, 27.4: 243-251.

VI. Multi-Radionuclide Digital Autoradiography of the Intra-Aortic Atherosclerotic Plaques using a Monoclonal Antibody Targeting Oxidized Low-Density Lipoprotein
Anders Örbom, Bo Jansson, Alexandru Schiopu, Susan Evans Axelsson, Jan Nilsson, Gunilla Nordin Fredrikson and Sven-Erik Strand
Manuscript

* Contributed equally to the paper

The work described in this thesis has been presented at the following international scientific meetings:

Society of Nuclear Medicine Annual Meeting 2006

IEEE Nuclear Sciences Symposium / Medical Imaging Conference 2007

Word Molecular Imaging Congress 2008, 2009, 2010 and 2012

Thesis at a glance

Paper I

Purpose: To characterize the imaging performance of a double-sided silicon strip detector (DSSD) system for digital autoradiography.

Methods: Measurement of detector efficiency, spatial resolution etc. using radioactive samples. Pilot animal study where multi-radionuclide imaging was employed.

Conclusion: A DSSD system can be successfully applied for digital autoradiography with multi-radionuclide imaging capability and has a spatial resolution that compared favorably to a storage phosphor system.

Paper II

Purpose: To investigate the distribution of ^{177}Lu-DOTA-BR96 monoclonal antibodies targeting the Lewis Y antigen over 7 days using a syngeneic rat model of colon carcinoma.

Methods: Biodistribution, digital autoradiography, histology and immuno-histochemistry of tumors from 38 rats at different times after injection of the radioimmunoconjugate.

Conclusion: The activity distribution to viable, antigen-expressing tumor cells is most efficient around 24 h post injection after which an increasing correlation between activity uptake and granulation tissue, interpreted as treatment effects, was observed.

Paper III

Purpose: To monitor cell death and activity distribution in tumors during the rejection process after treatment with a therapeutic activity of ^{177}Lu-DOTA-BR96.

Methods: Immunohistochemistry to detect cell death markers and digital autoradiography to image activity distribution in tumors from 21 treated and 9 control animals of the same type as Paper II.

Conclusion: Following radioimmunotherapy, tumor cells death occurred by a number of different mechanisms. Activity distribution over time was similar, but accelerated, compared to Paper II.

Paper IV

Purpose: To evaluate ICAM-1 as a potential target protein for in vivo imaging of advanced prostate cancer with radiolabeled antibodies.

Methods: Biodistribution, SPECT and PET/CT imaging, multi-radionuclide digital autoradiography, histology and immunohistochemistry of tumors from 29 mice with xenografts of human prostate cancer cells. Animals were injected with ^{111}In- or ^{177}Lu-labeled anti ICAM-1 or control antibody and some also with ^{18}FDG or ^{18}F-Choline.

Conclusion: Anti-ICAM-1 antibodies have potential for prostate cancer targeting, although observed poor tumor penetration and high activity uptake in the spleen will have to be further investigated.

Paper V

Purpose: To investigate the feasibility of targeting the free, unbound forms of prostate-specific antigen (PSA) for *in vivo* imaging of prostate cancer.

Methods: Biodistribution, multi-radionuclide digital autoradiography, histology and immunohistochemistry of tumors from 36 mice with xenografts of human prostate cancer cells. Animals were injected with ^{125}I-labeled anti free PSA antibody and some also with ^{18}FDG or ^{18}F-Choline.

Conclusion: Maximum tumor specific uptake of the antibody was observed 24 h post injection, although with higher specific retention in blood. Activity was distributed both to areas that stained positive for PSA and to necrotic areas, possibly an effect of the iodine labelling.

Paper VI

Purpose: To compare the different intra-aortic distributions of three radiolabelled tracers in an atherosclerotic mouse model.

Methods: Multi-radionuclide digital autoradiography, lipid staining and immunohistochemistry of mounted aortas from 12 atherosclerotic mice injected with ^{18}FDG and ^{125}I- or ^{131}I-labeled anti-oxidized Low Density Lipoprotein (oxLDL) and non-binding control antibodies.

Conclusion: Anti-oxLDL antibodies had a better plaque to aorta contrast than ^{18}FDG higher and uptake but not significantly different activity distribution compared to the control antibody.

Introduction

Preclinical molecular imaging

Small animal models play an important role as the stepping stone between *in vitro* research and clinical trials in the development of new diagnostic and therapeutic pharmaceutical agents and methods. Imaging, applied both *in vivo* and *ex vivo,* has come to constitute a crucial part of such preclinical studies. This is particularly the case for molecular imaging, which is defined by the Society of Nuclear Medicine and Molecular Imaging as:

> [The] visualization, characterization, and measurement of biological processes at the molecular and cellular levels in humans and other living systems. [2]

This is often achieved by using a tracer, visible to an imaging modality, that interacts with, or targets, a specific biological process. *In vivo* imaging of a live animal, often under anesthesia, allows longitudinal studies to be performed on the same animal, to study whether, for example, a candidate drug reaches its intended target, or if the pharmacokinetics may lead to unintended toxicity. In the case of radiolabelled tracers, *in vivo* imaging may also be used to estimate the absorbed dose to risk organs over time. *Ex vivo* imaging, on the other hand, often allows imaging at a spatial resolution that is orders of magnitude higher, and unhindered access to tissue for staining and observation. Both these imaging approaches are, therefore, integral parts of basic research and drug development [3].

In vivo imaging modalities

Non-radionuclide-based methods

Optical *in vivo* imaging has become increasingly popular as a high-throughput modality that does not require radioactive materials. The basic imaging technology employed is a charge-coupled device (CCD) that records the light emitted from the animal as a result of one of two processes. The first is bioluminescence, where cells, for example implanted tumor cells, have been engineered to express one of the luciferase enzymes and, upon the injection of luciferin, light will be produced in proportion to the amount of tumor cells, enabling tumor growth to be monitored.

The second process is fluorescence. A tracer with a fluorescent label is injected into the animal, and then excited with an external light source, and the lower energy light that is emitted is recorded. Multi-tracer imaging can be performed by using different fluorophores [4]. Optical imaging and radionuclide imaging can be combined by imaging the Cherenkov radiation that is emitted when charged particles are slowed down in tissue [5, 6].

In order to achieve anatomical imaging, which is often valuable as a reference to the images from other molecular imaging modalities, small-animal computed tomography (CT) can be used measure the attenuation of X-rays passing through the animal. Commercial systems can provide a spatial resolution of 50 μm, although the absorbed dose to the animal necessary for a high signal-to-noise ratio may be very high, on the order of 0.25 Gy for 135 μm voxels, affecting the animal's health or the outcome of the study [4, 7].

Dedicated small-animal magnetic resonance imaging (MRI) systems have the ability to achieve excellent soft-tissue contrast, and spectroscopy and functional imaging of perfusion, diffusion, etc., can be performed. Preclinical MRI systems have smaller bore-holes than clinical systems to accommodate a rodent, and commonly have higher-field magnets in the range of 4.7-11.7 T. A spatial resolution of 0.1 mm can be achieved while imaging live animals under anesthesia [4, 7].

Ultrasound imaging benefits from the smaller volume of animal models compared to humans, which allows for higher frequencies, thus providing better spatial resolution. Ultrasound biomicroscopy is an extension of this concept, providing a resolution down to 60 μm. Microbubble contrast agents, sometimes with targeting molecules on the surface, can also be employed [4].

Small-animal PET

Positron emission tomography (PET) is now a widely used imaging modality in the clinical setting, primarily in the field of oncology. The first PET systems specifically for rodent imaging were developed in 1995 [8], and today several systems are commercially available. In brief, a tracer radiolabelled with a β^+-emitter such as ^{18}F is injected into the animal, and upon decay a positron is emitted that eventually interacts with an electron, leading to the emission of two photons, each with an energy of 511 keV, in opposite directions to preserve momentum. These photons are then registered by a ring of detectors, each one usually consisting of a scintillator material and a photodetector. By recording only the events that are coincident in time, the position of the annihilation, somewhere between two detector elements, can be established, and a three-dimensional image of the activity distribution can be reconstructed [9]. The main benefits of small-animal PET are its high sensitivity, up to 100 times that of single-photon emission computed tomography SPECT, and accurate quantification, compared to other methods. The spatial resolution of commercial systems is currently around 1 mm. It is very common to combine small-

animal PET with CT to acquire anatomical information (Figure 1). The combination of PET and MRI is currently an active area of research and development [4, 7, 10].

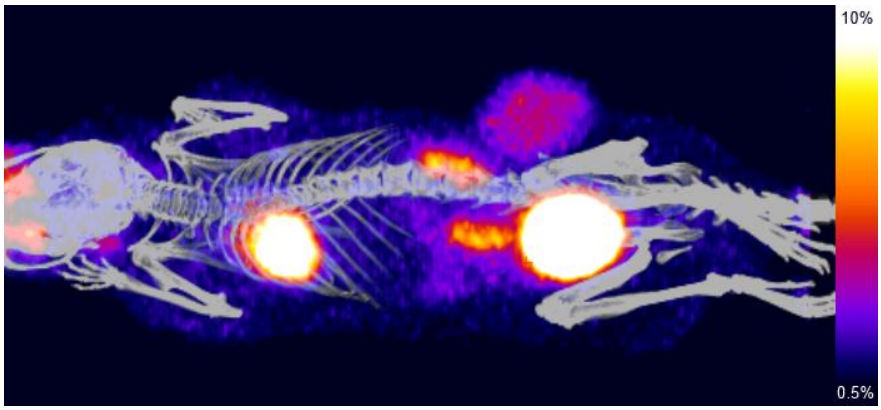

Figure 1.
A PET/CT maximum projection image of a mouse from the study described in Paper IV. This PET image was taken one hour after the intravenous injection of the metabolic tracer 2-deoxy-2-[^{18}F]fluoro-D-glucose (^{18}FDG), and scaled to 10% of the maximum voxel intensity in order to visualize other organs than the bladder, which contains most of the activity. Note the uptake in the heart and the subcutaneous tumor. A threshold was applied to the CT image to show only high-density voxels, i.e. bone.

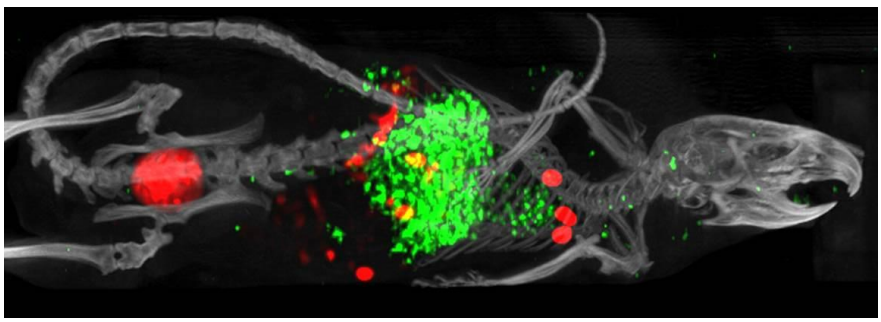

Figure 2.
A multi-radionuclide SPECT/CT maximum projection image of a normal mouse six hours after the intravenous injection of ^{111}In-trastuzumab (green) and ^{99m}Tc-Affibody (red). Note the uptake of trastuzumab in the liver and the concentration of Affibody in the bladder and mediastinal lymph nodes. (Image provided by Jonas Ahlstedt, Medical Radiation Physics, Lund University and Thuy Tran, Lund Bioimaging Center, Lund University.)

Small-animal SPECT

Single-photon emission computed tomography predates PET, and is in even wider use as a clinical imaging modality in a large number of diagnostic and therapeutic applications. While clinical SPECT systems have poorer spatial resolution than PET, for small-animal scanners the reverse is generally true, due to the use of pinhole collimators, although this results in lower sensitivity. To obtain the image, a tracer labeled with a γ-emitting radionuclide, such as ^{99m}Tc or ^{111}In, is injected into the animal and, at the desired point in time, the anesthetized animal is inserted into the SPECT camera. The detectors, which are either stationary or rotate around the animal, usually consist of scintillation detectors coupled to photodetectors, classically photomultiplier tubes. Semiconductor detectors have also been used in preclinical systems and are being developed due to their small pixel sizes and excellent energy resolution [11]. Collimators are placed between the animal and the detectors, and in modern small-animal systems these are typically multiple-pinhole type collimators. These allow for small objects to be projected onto the larger detector, improving the spatial resolution compared to classical parallel-hole collimators. The pinhole size determines the trade-off between spatial resolution and sensitivity. Adding additional pinholes increases the sensitivity, although the images projected onto the detector will overlap, which may degrade the reconstructed image [12]. Using this technology, sub-millimeter spatial resolution can be achieved, at least for smaller areas of the animal. Activity quantification has classically been difficult using SPECT, and corrections for photon attenuation and scatter must be included in the reconstruction algorithm to improve the quantitative accuracy [7].

Unlike PET, the radionuclides used for SPECT tracers emit γ radiation at many different energies, and this can be employed to image several tracers simultaneously (Figure multi-SPECT), for example, both blood flow and a molecule targeting a specific antigen. Algorithms to correct for cross-talk between the radionuclides present as well as down-scatter from the higher energy emitter are then employed to produce separated images [4, 13]. As with small-animal PET systems, a CT scanner is commonly included in small-animal SPECT [7].

Ex vivo imaging modalities

Non-radionuclide-based methods

Tissue samples taken from sacrificed animals or in the form of biopsies can be studied using a range of imaging techniques. The most common is light microscopy of samples stained, for example, with hematoxylin and eosin to reveal the histology of a tissue section. More advanced staining can be performed using immunohisto-chemistry, in which a thin tissue section is exposed to a solution of antibodies targeting a specific antigen. This antibody either carries a reporter molecule, or it is carried on a secondary antibody, which adheres to the primary antibody, in an effort

to amplify the staining. This reporter can be an enzyme which, upon incubation, converts a chromogenic substrate into a visible colored substance. A variation of this method is immunofluorescence, where the reporter is a fluorophore and the sample is imaged using a fluorescence microscope. The spatial resolution of light microscopy is commonly reported as being down to 0.2 μm [14].

Many histological staining techniques can be adapted for electron microscopy, which is able to reach sub-nanometer spatial resolution, but requires more extensive preparation of very thinly sectioned tissue samples. The two main technologies are the transmission electron microscope, which measures the attenuation of an electron beam traversing the sample, and the scanning electron microscope, in which the electron beam scans the sample surface and the resulting secondary electrons, light or x-rays are detected. Electron microscopy can be combined with radionuclide imaging in electron microscopic autoradiography, which is analogous to micro-autoradiography described below [15, 16].

A technique that has undergone significant development recently is mass spectrometric imaging (MSI). The main benefits of this compared with other methods are that there is no need of a label that might change the biological behavior of the injected compound, and the ability to measure both the original compound and any metabolites. The two main methods used are matrix-assisted laser desorption/ionization MSI and secondary-ion MSI; the former typically being used to image larger samples at a sub-millimeter resolution, and the latter for smaller samples with sub-micrometer resolution. The drawbacks of MSI compared, for example, to autoradiography are the long preparation and handling time of samples and the lack of accurate quantification of the measured compounds [3].

Autoradiography

Autoradiography can be said to be the first imaging technique ever used for the localization of radioactivity in a sample with the darkening of a film when Henry Becquerel discovered radioactivity, and images of biological samples were produced as early as 1904 [3]. Autoradiography is actually a number of technologies and methods used to produce a two-dimensional image of the distribution of activity in, or on, a thin, solid and immobile sample, that is in close proximity to the detector or detection medium [3, 17]. The images are formed by the charged particles emitted (α or $\beta\pm$), while γ radiation often passes through the detector without interacting with it [18]. Apart from superior sensitivity and quantification compared to other methods, autoradiography is vital for dosimetry at the cell and tissue levels since it images the actual interactions delivering the absorbed dose.

Traditionally, autoradiographic film has been used, the spatial resolution of which is limited only by the 0.1–0.4 μm size of the silver halide crystals that compromise the detection medium [19]. However, film has a number of drawbacks: it does not show a linear response to different levels of activity, the dynamic range is limited, and the

sensitivity is low, often requiring weeks of exposure per sample [3, 17, 19]. Photographic emulsion is, however, still widely used for micro-autoradiography in which the tissue sections are in direct contact with the photographic emulsion, either by mounting them on pre-coated slides, or by applying the emulsion to the slides after sectioning [3, 17]. After exposure and development the tissue is studied using light microscopy and very high-resolution, although not quantitative, data on the activity distribution can be obtained.

Since macro-autoradiography on the 100 µm scale is sufficient in many applications, and the ability to acquire quantitative images is of high priority, the technology that has replaced film as a standard method is storage phosphor screens. When exposed to ionizing radiation, BaFBr:Eu^{2+} phosphor crystals absorb the energy of interacting particles and are oxidized to BaFBr:Eu^{3+}; the electron being trapped in the crystal matrix. During read-out, a red laser releases the electrons, Eu^{3+} is reduced to Eu^{2+}, and the energy is released as visible blue light that can be quantified using a photomultiplier tube [20]. A spatial resolution of 60 µm was reported for storage phosphor systems in the International Commission on Radiation Units and Measurements (ICRU) Report 67 in 2002 [17].

However, neither film nor storage phosphor systems provide any real-time information on the progress of imaging, and neither records the time of interaction of each detected particle [17, 19]. A number of digital autoradiography systems, based on different detector technologies, have therefore been developed to address these shortcomings and, if possible, improve the spatial resolution.

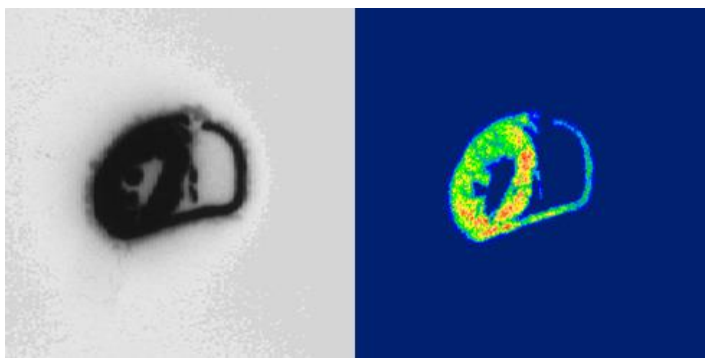

Figure 3.
Autoradiographic images of a tissue section from the heart of a rat injected with ^{99m}Tc-hexamibi. Left: autoradiographic film after 24 hours of exposure. Right: the image obtained after 30 min using the beta camera autoradiography system developed by Ljunggren et al. [21]. (Image provided by Sven-Erik Strand, Medical Radiation Physics, Lund University.)

Solid-state, silicon detectors have also been developed, some based on back-thinned CCD and complementary metal oxide semiconductor (CMOS) sensors [22, 23], or silicon pixel detectors [24]. Silicon strip detectors, such as that used in the present work, have also been employed in earlier systems, although the intrinsic spatial resolution was lower [25, 26].

Among these, are systems using a CCD to register the scintillation light generated by the radioactivity in a sample in either a sheet of scintillator [27], a thin layer of phosphor [28], or in a parallel-plate avalanche chamber [27]. A notable recent system is the α-camera, which uses sheets of silver-activated zinc sulfide phosphor, upon which tissue sections containing an alpha particle emitter are directly mounted, and the resulting scintillation light is collected using a cooled CCD and a magnification lens [29]. Another technology, Microchannel plates, have been employed in several systems, among them the beta camera developed by Ljunggren and Strand (Figure 3), based on a thin scintillator, the photoelectrons from which are amplified by a microchannel plate and registered by a resistive anode [21, 30].

Image-based dosimetry

In order to evaluate and predict the biological effects of a specific exposure to radiation, especially in therapeutic applications, *dosimetry* is employed. The absorbed dose (D) is defined as

$$D = d\varepsilon / dm \qquad \textbf{Eq. 1}$$

where $d\varepsilon$ is the energy deposited by ionizing radiation in a volume element with the mass dm [17]. Internal dosimetry, which is used to calculate the absorbed dose delivered by radionuclides inside the body, requires knowledge of the activity, location, and behavior of these radionuclides over time.

Macroscopic dosimetry

The US Society of Nuclear Medicine's Medical Internal Radiation Dose (MIRD) Committee has developed a system for internal dosimetry that has become the standard for medical applications [31, 32]. In this system, the absorbed dose in target region k from source region h is defined as:

$$D_{k \leftarrow h} = \tilde{A}_h S_{k \leftarrow h} \quad \text{Eq. 2}$$

where $\tilde{A}_h$ is the accumulated activity in the source region, and the S value $S_{k \leftarrow h}$ represents the mean dose deposited in k from each unit of accumulated activity in h. S values are typically employed at the organ level, where they have been determined for different radionuclides through the use of computational phantoms representing reference humans [33]. However, if activity data are available at better than organ-level resolution, voxel S values can be used. These are determined by calculating the amount of energy that is deposited in a voxel of a certain volume at a certain distance from the decay of a specific radionuclide in a homogeneous tissue-equivalent medium [34].

The MIRD approach is applicable in both clinical and preclinical dosimetry, and calculations of S values have been performed for different animals, such as mice [35] or rat [36]. In both clinical and preclinical dosimetry, the activity data for organs or voxels may come from *in vivo* imaging modalities such as PET or SPECT, preferably with repeated or dynamic measurements to correctly quantify the accumulated activity [33]. However, the MIRD method has two major limitations: first, it is a generalized method that does not take into account the individual anatomy of the patient, and second, while voxels may be of any size, the activity data will have the same resolution as the imaging modality [37]. The first problem can be addressed by using the three-dimensional accumulated activity distribution from the individual animal or patient to directly calculate the absorbed dose distribution.

If it is assumed that the activity is distributed throughout a homogeneous medium, dose point kernels (DPKs) can be convolved with the accumulated activity distribution to calculate the absorbed dose distributions. A DPK is either analytically calculated or simulated using Monte Carlo techniques, and contains the absorbed dose at all locations within the kernel diameter around the decay of a specific radionuclide [33, 37]. If the medium cannot be assumed to be homogeneous, as in the case of bone or lung dosimetry, the activity distribution from PET or SPECT and the density map from a CT scan can be employed to perform a more accurate, if time-consuming, Monte Carlo simulation of the energy deposited by the radionuclides [33, 38].

Small-scale dosimetry

While both clinical and preclinical PET and SPECT provide sub-organ resolution, they do not fulfill the requirement of imaging the activity distribution on the scale of the range of the charged particles delivering the absorbed dose [37]. For lower energy β-emitters and especially for α-emitters with ionization ranges of a few μm, decay on the cell surface or in the cell nucleus may be of great importance regarding the

biological effect [39]. A system for cellular S values has been developed in order to investigate the effect of sub-cellular localization for different radionuclides [37]. Heterogeneous activity uptake inside organs or regions of organs that may be visible using *ex vivo* but not *in vivo* modalities has been shown to introduce errors when the MIRD assumption of sub-region homogeneity is applied [17, 40]. The risk of erroneously calculating mean absorbed doses is that the absorbed dose will not be correlated to the biological response, and will affect, in particular, individualized therapy planning. An approach proposed to address this problem is the development of models that can relate the measured mean activity level to an assumed sub-voxel distribution acquired from preclinical data and biopsies [41, 42]. This will allow the approximate calculation of the absorbed dose to the actual radiosensitive tissues or even to the nucleus of the cells if the model considers that scale [39]. Autoradiography is at present the only imaging modality capable of resolution comparable to the range of charged particles, and will therefore be a main tool for providing the parameters required in small-scale dosimetry models for individual radiopharmaceuticals. Most autoradiography systems will be capable of resolving regional heterogeneity in a tumor or normal tissue, however, micro-autoradiography will be needed to determine the distribution of radionuclides at the cellular level, especially for α-emitters and radionuclides with dominant Auger emission [17]. While the application of small-scale dosimetry in the clinic will be a challenge, as activity distributions will, at best, be known in sub-organ voxels, the prospects in preclinical studies of new radionuclide therapies are better, as high-resolution *in vivo* an *ex vivo* imaging data can be combined with *in vitro* results to obtain more accurate dosimetry [37].

Aims of this work

The overall aim of the studies included in this doctoral thesis was to evaluate the potential of digital autoradiography with multi-radionuclide imaging capabilities to contribute to preclinical studies employing radiolabelled targeting molecules. This included characterizing the capabilities of the detector system itself, as well as applying it to studies using animal models, in the pursuit of new targeting molecules for both diagnostics and radionuclide therapy. The specific aims of each paper in relation to this overall aim were:

- to characterize the performance of a newly developed commercially available double-sided silicon strip detector system for autoradiography, and test its application in a dual-tracer preclinical pilot study (Paper I),
- to investigate the activity and the distribution of the absorbed-dose rate of the radiolabeled antibody ^{177}Lu-DOTA-BR96 within tumors at different points in time in relation to histology, antigen expression, and vascularization (Paper II),
- to repeat the study performed in Paper II but at therapeutic instead of sub-therapeutic levels of activity, and to relate these results to staining of cell death markers in tumors during the therapeutic process (Paper III),
- to make the first evaluation of the targeting potential and biodistribution properties of a radiolabeled antibody targeting the protein ICAM-1 in a prostate-cancer-based model using small-animal SPECT/CT, multi-radionuclide digital autoradiography, and *ex vivo* biodistribution (Paper IV),
- to investigate the feasibility of targeting the free, unbound forms of prostate-specific antigen with an ^{125}I-labeled antibody, using *ex vivo* biodistribution and multi-radionuclide digital autoradiography (Paper V), and
- to simultaneously compare the distribution of ^{18}FDG and ^{125}I/^{131}I-labeled anti-oxidized low-density lipoprotein and control antibodies in an atherosclerotic mouse model using multi-radionuclide digital autoradiography (Paper VI).

The digital autoradiography system

The same commercially available digital autoradiography system, the Biomolex 700 Imager (Biomolex, Oslo, Norway), was employed in all the work presented in this thesis. The system is based on a double-sided silicon strip detector (DSSD), which has advantages and disadvantages compared to other systems. The studies were carried out using the same unit (at the Lund University Bioimaging Center, LBIC) except for the multi-radionuclide study of tumor penetration using two different tracers presented in Paper I, where a prototype of the system at the University of California, Los Angeles was used.

System design

The semiconductor detector element provides much better energy resolution than that obtained with scintillation-based detectors due to the large number of electron-hole pairs created when ionizing radiation interacts with the detector. These act as information carriers for the energy measurement providing better statistics than the smaller number of photoelectrons that serve the same purpose in a scintillation detector [43].

The system used in this work is based on a DSSD with 560 x 1260 parallel silicon strips, with a pitch of 50 µm, on each side of a 300 µm thick n-doped silicon wafer, which acts as a depletion area. The strips on the two sides run orthogonal to each other and are p^+-doped or n^+-doped. They are connected to read-out electronics via aluminum contacts. When a voltage difference is applied over the detector each strip operates as a reverse-biased diode. Electron-hole pairs are created by incoming radiation in proportion to the energy deposited, and a current can be read out from the strips closest to the point of interaction [44]. The detector design is illustrated in Figure 4.

The detector is cooled by a Peltier element and a fan to 20°C during operation, and the energy threshold for detection is between 15 and 30 keV, depending on the specific detector unit. The readout electronics consists of a dedicated, self-triggering CMOS chip that reads out the coordinates and the energy of a detected event in the microstrip detector. These data are sent in real time to software running on a

computer connected to the system. After imaging, the data can be exported in binary format or in list mode as a text file.

A charged particle can have a torturous path through a silicon detector, depositing energy at several locations before all its energy is deposited. This will cause degradation of the spatial resolution, and different systems employ different mathematical algorithms to determine the point of origin of the particle [24]. In the system used in this work, the strip on either side of the detector reporting the highest current during the measurement period (≥ 10 µs) determines the coordinates. The detector thickness affects the spatial resolution, in that a thicker detector will be more sensitive to particles depositing energy over several pixels [19], limiting the maximum energy that can be measured of a β particle traversing the detector in a straight line. Electrons with an energy above 229 keV would have a longer continuous slowing down approximation (CSDA) range than the thickness of the detector (300 µm), allowing them to pass through the detector without depositing all their energy [18]. For electrons and positrons with higher energies, the detector will measure the energy deposited per unit distance travelled and, as can be observed in Figure 5, the total mass stopping power for electrons in silicon is comparatively constant between approximately 0.3 and 5 MeV. This results in the measured energy spectra of medium- to high-energy beta emitters being very similar.

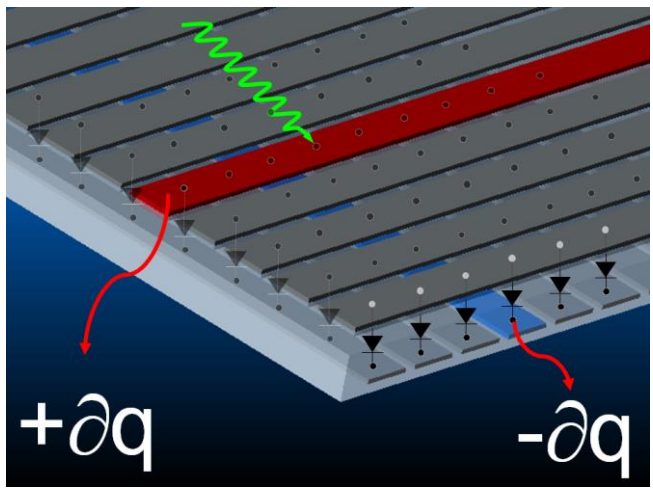

Figure 4.
Illustration of the detection principle of the double-sided silicon strip detector. Electron-hole pairs are created in proportion to the energy deposited at the point of interaction, and a positive and negative current can be detected through the strips on either side of the detector, yielding information on both the location of the event and the energy deposited. (Image © Biomolex AS, Oslo, Norway.)

The preparation of samples for imaging in the autoradiography system consists of placing them on a standard 75 mm × 25 mm microscope slide. The slide is then placed in a plastic sample holder and covered with a 3 µm Mylar foil before being loaded either manually or through a 12-slot sample changer into the instrument, where it is gently held against the detector from below.

System characteristics

The characteristics of the detector were evaluated with regard to spatial resolution, detection efficiency, measurement of energy spectra, system dead time, and background noise (Paper I). All tests were performed using the same equipment that was used for the majority of digital autoradiography studies presented in Papers I-VI.

Spatial resolution

The spatial resolution of an autoradiography system will depend on the energy of the particle that is detected, as the particle will deposit energy continuously along its path through the detector [24]. Different radionuclides will therefore give rise to different point spread functions in the detector, and higher-energy charged particles will result in more blurred images than lower-energy particles of the same type. This also leads to difficulties in comparing different systems, since the spatial resolution will differ depending on the radionuclide and the methodology employed.

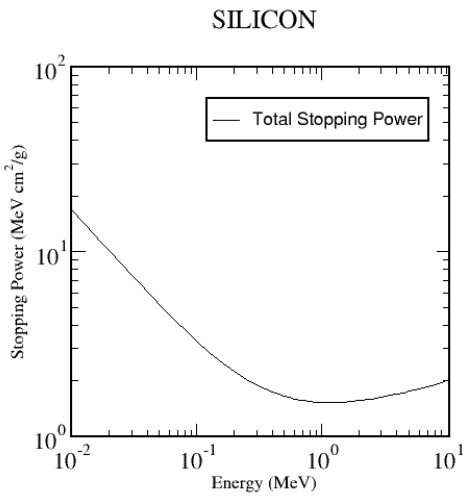

Figure 5.
The total mass stopping power for electrons in silicon at different energies [45].

The spatial resolution of an autoradiography detector can be measured in a number of ways. A common method is to image a radioactive source with a physically sharp edge, and to fit an integral of a Gaussian distribution to the profile of this edge, and then calculate the full width at half maximum (FWHM) of the distribution [24, 46]. However, this method was not employed in the study described in Paper I, partly due to the difficulty in manufacturing a sharp-edged plane source. Collimating a plane source with shielding material was not possible either, as the DSSD system did not allow direct access to the detector.

The spatial resolution of a detector can, however, be measured directly using a point source or a line source with a significantly smaller diameter than the intrinsic resolution of the detector [21, 29, 47]. In order to produce a thin line source a pure nickel wire was used which, according to the manufacturer (Alfa Aesar, Karlsruhe, Germany) had a purity of 99.98% and a diameter of 10 µm. Nickel is naturally mostly ^{58}Ni, and exposure to fast neutrons leads to the formation of the isotope ^{58}Co through the interaction ^{58}Ni(n,p) ^{58}Co. ^{58}Co has a half-life of 70.86 days, and is a both a β^+-emitter (14.9%, mean β^+-energy 201.1 keV) and a γ-emitter (99.4%, γ-energy 810.8 keV).

The wire, 1 m long and kept on its original spool, was irradiated at FiR 1, located in Espoo, Finland, which is a Triga Mark II research reactor with a nominal power of 250kW. The nominal power of the FiR 1 research reactor is 250 kW. The neutron flux for thermal and fast neutrons in the water filled central thimble in the middle of the reactor core, where the nickel wire was irradiated, is approximately 1.0×10^{13} neutrons cm^{-2} s^{-1}. The total irradiation time was 18 hours divided on 4 separate occasions during May and June 2013.

The wire was very embrittled by irradiation in the reactor, and had to be transferred from the spool by pressing pieces of pressure sensitive adhesive tape onto the spool and quickly removing them, carrying segments of the wire on the adhesive side of tape, which was then mounted facing the detector. The wire segments were imaged using light microscopy and found to have a diameter of 18.0 ±1.8 µm, the widening probably partly resulting from mechanical stress during the transfer. In order to confirm the radionuclide content, the radiation from the wire was measured for 14 days using high-resolution gamma spectroscopy with a High-purity Germanium detector (Canberra SeGe, model GC5021, Canberra, Meriden, Connecticut, USA) placed behind a lead shield. Apart from ^{58}Co, the other radioisotopes detected were: ^{57}Co, ^{60}Co, ^{59}Fe, ^{57}Ni and ^{51}Cr, all of which except ^{58}Co had a relative intensity below 0.1 percent.

A matrix of wire segments was imaged using the DSSD system (for 93 h), and a storage phosphor screen (Cyclone Plus, Perkin Elmer, Wellesley, MA, USA), for 144 h, for comparison. The DSSD image was reconstructed. ImageJ software [48] was used to subtract the background not due to ^{58}Co from both images (Figure 6) before measuring intensity profiles over the line sources to determine the FWHM.

The mean FWHM based on measurements from 5 line profiles per image was 154 ±15 µm for the DSSD system and 344 ±14 µm for the storage phosphor screen. This can be compared to FWHM values for ^{14}C ranging from 20 µm for a system based on contact imaging through a solid scintillator sheet [27] to 79.5 µm for a CMOS-based system [49], as reported in a paper by Esposito et al. from 2011 [24]. However ^{14}C has a lower mean beta energy of 49 keV, compared to 201 keV for ^{58}Co, which will result in a shorter CSDA range and a smaller FWHM.

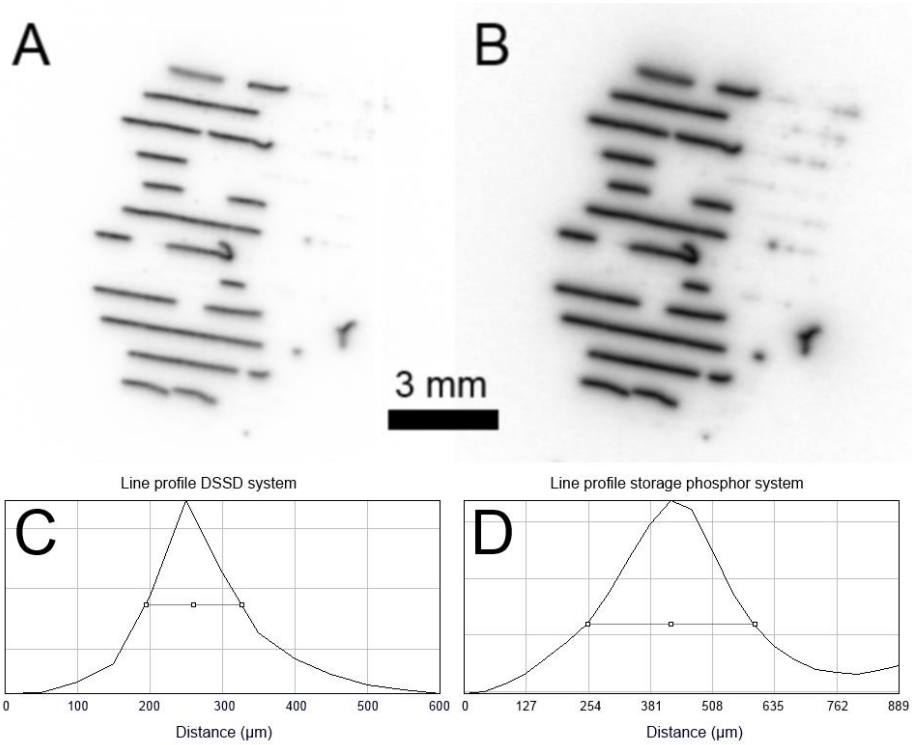

Figure 6.
Top: Digital autoradiography images of the same sample consisting of segments of 18 µm thick wires, showing the ^{58}Co activity obtained with the DSSD system for 93 h (A), and a storage phosphor screen system for 144 h, which was scanned at 600 dpi (B). Background was subtracted, and both images were individually scaled from zero (white) to maximum (black) intensity. Bottom: Examples of intensity line profiles from one of the lines in the images above, measured using the DSSD system (C) and the storage phosphor screen (D).

Detection sensitivity

The detection sensitivity was measured for the following commonly used radionuclides: ^{99m}Tc, ^{111}In, ^{177}Lu, ^{125}I, ^{131}I, ^{18}F and ^{68}Ga. A tissue homogenate was mixed with radionuclide solution, frozen and cryosectioned at a thickness of 10 µm. For each radionuclide, 5 sample slides, each with 3 sections, were imaged for at least one hour, and the initial count rate calculated. Sections adjacent to those imaged were dissolved in acid and the radiation measured in a well-type gamma counter (Wallac WIZARD 1480, Wallac, Turku, Finland). The mean activity per section was then divided by the mean count rate corrected for radionuclide decay, and the sensitivity was calculated as counts per second per kBq, as given in Table 1. Note that the sensitivity is only valid for a particular detector due to differences in calibration and energy threshold.

Table 1. Detection sensitivity of the DSSD autoradiography system for selected radionuclides.

	^{99m}Tc	^{111}In	^{177}Lu	^{125}I	^{131}I	^{18}F	^{68}Ga
Sensitivity (cps/kBq) ±SD	74±3	227±8	599±49	249±13	229±10	334±37	153±21

Energy spectra

The energy spectra were recorded simultaneously with the sensitivity measurements from 10 keV to 500 keV and are shown in Figure 7, where they are individually scaled to the maximum intensity.

Environmental background and noise

In order to determine the background, a microscope glass without a sample was imaged in the detector for 52 hours. The image was reconstructed and the total number of counts determined. The total background was 1.177 counts per second, homogeneously distributed over the entire image. This is equivalent to 1.811×10^{-6} counts per second per pixel. The measured energy spectrum of the background is shown in Figure 8.

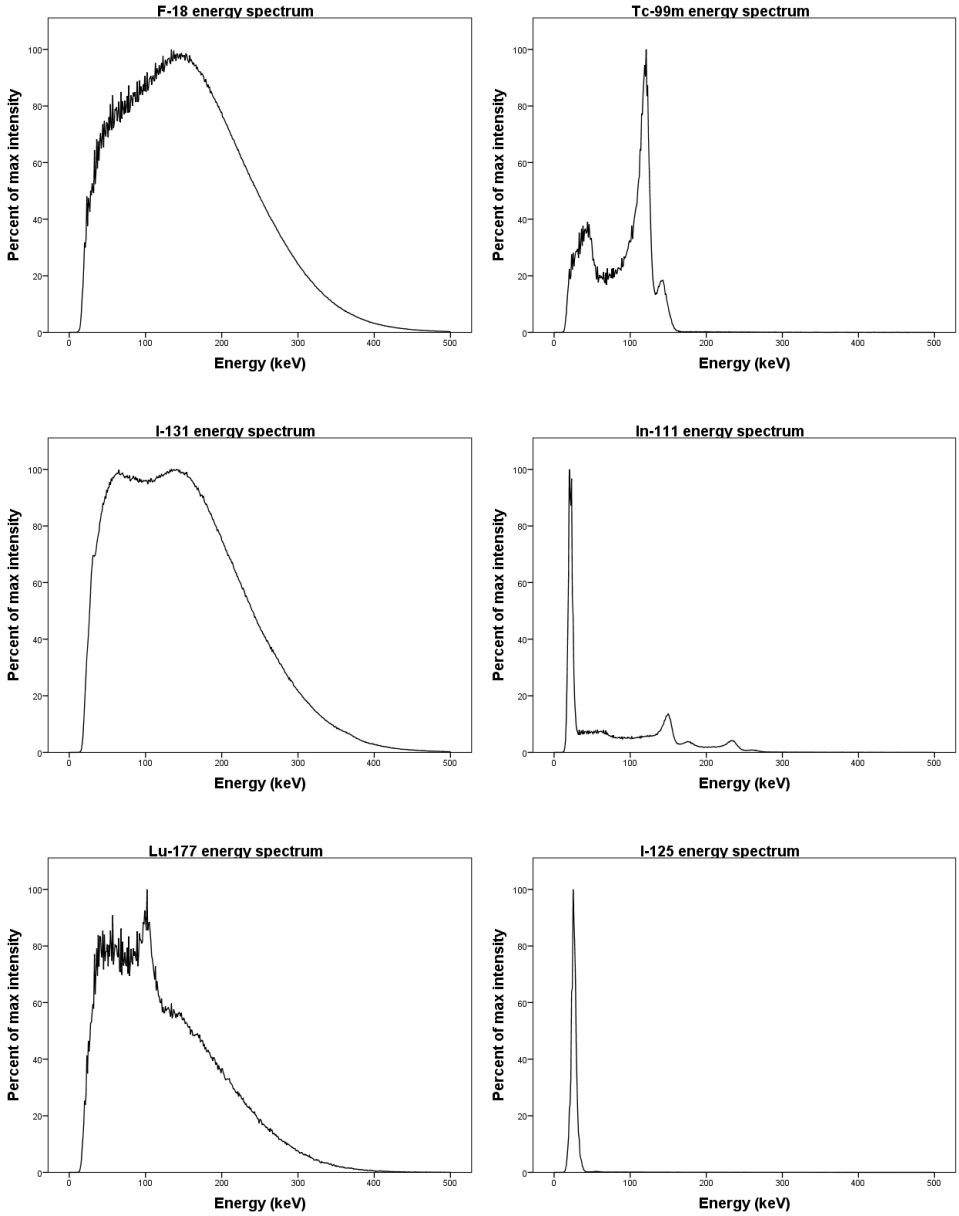

Figure 7.
Selected energy spectra measured with the DSSD autoradiography system, individually scaled to the maximum intensity.

System dead time

The dead time of a detector is the time after each event during which the system is not able to record another event. This will result in events being lost if the count rate is too high [43]. To determine the dead time for this system, two ^{18}F samples of approximately 5 kBq and 7 kBq were imaged on separate occasions for the full time it took them to decay. Since a nonparalyzable system behavior was observed when plotting the count rate over time from the max measured level of 4000 counts per second, the following model was used to determine the system dead time τ:

$$n = m / 1\text{-}m\tau \qquad \textbf{Eq. 3}$$

where m is the measured count rate and n the expected count rate determined from results at low (<100 counts per second) count rates. The model was fitted to the data and the system dead time, τ, was found to be 59 µs (R^2=0.995).

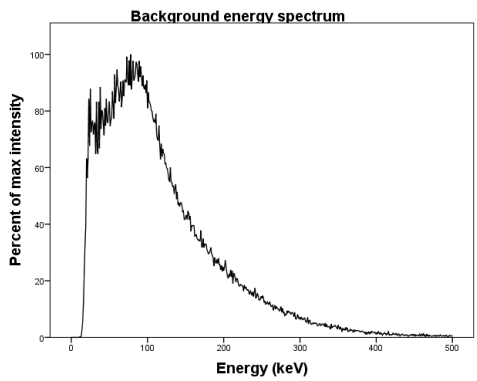

Figure 8.
The background energy spectrum measured with the DSSD system when a microscope slide without a radioactive sample was imaged for 52 hours.

Image reconstruction

Data were exported from the digital autoradiography system in list-mode format, with each line in the text file consisting of the x and y coordinates and the energy measured for each detected event. In the studies presented in Papers I-V and part of Paper VI the total number of events detected by the instrument was also recorded in a text file once per minute. These two files were used as input for the software developed exclusively for these projects using the programming tool IDL 6.4 (ITT Visual Information Solutions, Boulder, CO, USA). Four one-dimensional arrays with as many elements as detected events were created from the data, each containing at corresponding positions either the x or y coordinate, the measured energy or the time in minutes after imaging was started. These arrays were then used to control the data, for example, to select for a specific range of energies or points in time, while maintaining the discrete character of each event.

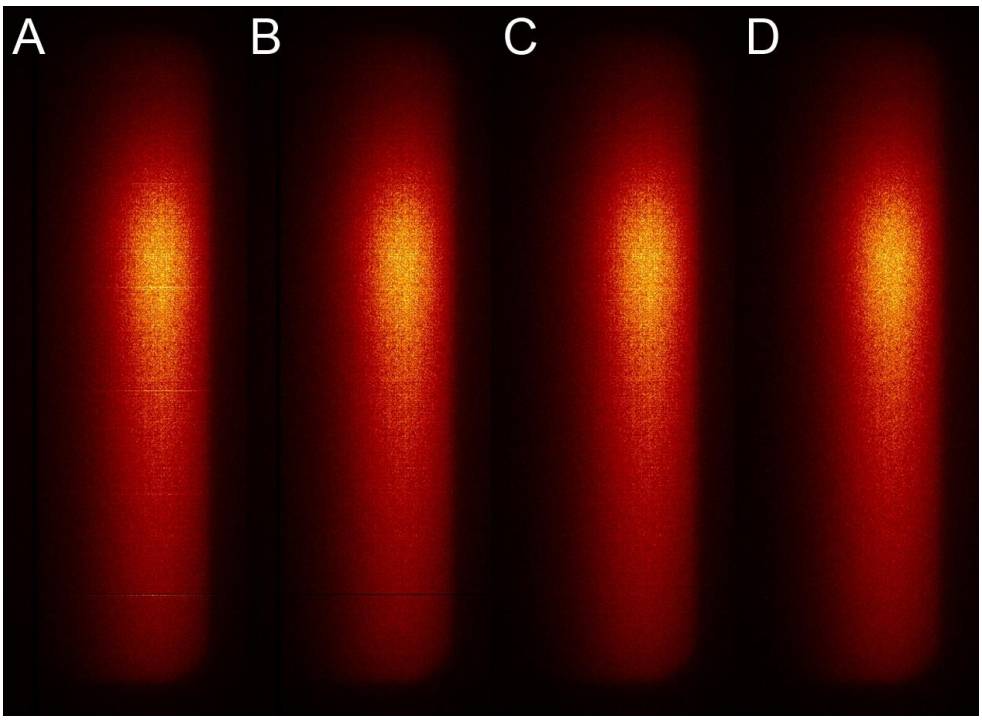

Figure 9.
An image of a natural yttrium foil activated in a cyclotron with 45 μA, 12.8 MeV protons to give ^{89}Zr. From left to right, an uncorrected image (A), with corrections for known miscalibrated strips (B), with corrections for faulty or over-reporting strips (C), and with corrections for minor differences in strip calibration (D). Individually scaled from zero (black) to maximum (yellow) intensity. (Activated foil courtesy of Jonathan Siikanen, Medical Radiation Physics, Lund University.)

A number of optional corrections could be applied using the software. Initially, the number of counts in strips that had been empirically identified as over- or underreporting the activity due to differences in calibration were corrected by either deleting a pre-specified fraction of the detected counts at random, or conversely, by duplicating counts selected at random (Figure 9B). Silicon strip detectors with a very small pitch will almost always have a number of strips where the connection to the read-out electronics has either failed completely or results in such a high level of noise that the signal from the strip must be removed so that it does not contribute to the collected data. Interpolation was employed to deal with these faulty strips. In the case of a single faulty strip, half the counts were randomly selected from each nearest neighbor and combined to recreate the missing signal. In the case of two adjacent faulty strips, one third of the counts from the furthest functioning strip was combined with two thirds of the directly neighboring strips to replicate the missing signal, and so on for different configurations of faulty strips (Figure 9C).

For biological samples, the profiles of the total counts projected on the x and y axes can be expected to be smooth, since the edges between areas of different types of cells are not very sharp at the resolution of the detector. Most of the noise in the profile can therefore be attributed to slight variations in strip calibration, and to correct for this, a simple mean-value filter was convolved with each of these profiles. The ratios between the original profiles and the smoothed ones for each row and column were used as a correction factor to either randomly reduce or randomly duplicate events so as to decrease or increase the signal from each strip (Figure 9D).

After performing the necessary corrections, the image is reconstructed as a two-dimensional histogram of the x and y coordinates. At this point, the pixel intensity can also be scaled using calibration factors to give the activity in Bq per pixel or percent injected activity per gram (%IA/g) per pixel. In the latter case, the injected activity was known from previous measurements and the weight of tissue per pixel was determined by comparing the area of a section in the digital autoradiography image with the area of the same section scanned using light microscopy multiplied by the section thickness and an assumed density of 1.0 g/cm^3. Images were saved as either integer or floating point matrices in the Interfile data format [50].

Separation of multiple radionuclides

Using samples containing two radionuclides with significantly different half-lives and imaging them twice, before and after decay of the short-lived isotope, is a fairly common method to separate their contributions to an autoradiography images. In some such studies, the contribution of the long-lived radionuclide to the first image is very small, and no separation is considered necessary [51-54]. An early example of the separation of the contributions of different radionuclides according to their energy

deposition was published in 1966 by Wimber et al., who compared the visible tracks of ^{3}H and ^{14}C in layers of film emulsion [55]. Separation of ^{35}S and ^{32}P using storage phosphor plate screens by imaging with and without an attenuating filter between the sample and imaging plate has also been reported [56]. The separation of radionuclides by energy after a single imaging session has been demonstrated in modern digital autoradiography systems using the scintillation light from a scintillator sheet in contact with a sample, or by using a parallel-plate avalanche chamber [27]. Semiconductor detectors have a better energy resolution than scintillation detectors, and successful separation of ^{35}S and ^{32}P has been shown on a DSSD system similar to but predating the instrument used in this work [57].

The separation methods employed in the present work vary depending on the radionuclide and application. The software used to separate the activity contributions was specifically written or adapted for each project. For simultaneous imaging of two radionuclides with sufficiently different energy spectra, a simple ratio between two energy windows can be used to calculate the ratio between the radionuclides in one pixel. This method was presented for the separation of ^{125}I and ^{131}I, using one energy window including the ^{125}I peak and one not including this peak, by this author in an earlier publication [58]. Both the simulation of separation of artificially mixed single radionuclide energy spectra and a phantom measurement were performed. From the simulated separation it was found that for a pixel with a total of 100 counts, the average error of $^{125}I/^{131}I$ separation was less than 5%. The phantom measurement and separation of the same radionuclides can be seen in Figure 10.

The method described above was applied in the study presented in Paper I. Only energy separation was employed since temporal resolution of the data had not yet been implemented in the read-out software, and only one imaging session was performed per sample. In a later study (Paper IV) tissue sections containing ^{177}Lu (half-life 159.5 h) and ^{18}F (half-life 1.8 h), both β-emitters, were imaged. While good quality ^{177}Lu images are easily obtainable with longer imaging sessions once ^{18}F has decayed, a mixed image is required for the separation of ^{18}F from ^{177}Lu. The energy spectra of these radionuclides are too similar to employ energy separation, so the temporal distribution was used by comparing the total number of events in the first hour of imaging to the total number of events in the next hour or longer, depending on imaging duration. The software was used to iteratively determine which contributions of the events from each radionuclide in the first time window best matched the total in the second time window, per pixel. This was done at a reduced spatial resolution of 100 µm pixel size in order to increase the statistics. Phantom measurements were performed under the same conditions as the biological samples, and showed that ^{18}F was overestimated by 3% in an mix of equal activities, and that 89% of a pure ^{18}F sample is correctly classified as only ^{18}F (see Paper IV for details).

In the study described in Paper V, ^{18}F and ^{125}I were used, which allowed separation based on both the measured energy spectra and the differences in half-life. This was achieved by imaging once, directly after sectioning and from this image separating ^{18}F

and ^{125}I by energy in the same manner as ^{131}I and ^{125}I, described in Paper I. To obtain a detailed ^{125}I image the sections were also imaged for a longer period after ^{18}F had decayed.

In the study presented in Paper VI, three radionuclides, ^{18}F, ^{131}I and ^{125}I were separated, and again two imaging sessions were employed for each sample, one before and one after ^{18}F decay. ^{131}I and ^{125}I were separated using the latter image, as described in Paper I, but in order to separate ^{18}F, two different methods were employed since at the time of the first study reported in Paper V, temporal resolution of the imaging data had not yet been implemented in the system. An additional complication was that the images had been acquired at count rates where dead time led to missing counts, and the image collected after the decay of ^{18}F could not be back-corrected to that collected before the decay of ^{18}F in a straightforward manner. Therefore, the distinct peak of ^{125}I was used as a reference and the total number of counts from each radionuclide was estimated by calculating what the ratio of ^{125}I and ^{131}I would have been in the initial image (before ^{18}F decay) from the data in the image after ^{18}F decay. After smoothing both the initial image and the separated ^{131}I and ^{125}I images with a 5 x 5 pixel mean filter, the two iodine images were subtracted from the initial image leaving only ^{18}F. In the second study, where temporal data were available, a simpler method could be used to remove the counts due to ^{125}I from the initial image by using events with an energy over 40 keV, after which ^{18}F and ^{131}I could be separated in the same manner as described in Paper IV.

The successful separation of ^{18}F, ^{177}Lu and ^{99m}Tc using a single measurement has also been presented (Poster by Örbom et al. at the World Molecular Imaging Congress 2010). In this case, three pure samples of each radionuclide were placed beside each other and then imaged. Separation was performed using both energy and time windows in each pixel. Powell's numerical optimization algorithm was then employed to find the distribution of events between the three radionuclides in each pixel that best fitted the distribution of the measured data between different windows [59]. The initial and separated image can be seen in Figure 11.

The software for radionuclide separation supplied with the DSSD system is intended mainly for protein kinase microarray imaging, and has not been analyzed as part of this present work. An initial version of the software employed a least-squares fitting method for separation based on energy windows, which was determined to be almost as effective as a more time-consuming maximum-likelihood algorithm developed by Kvinnsland and Skretting [57]. However, in a recent software update, a more efficient maximum-likelihood method, outlined in a report by the Norwegian Computing Center in Oslo, has been implemented, which uses time windows as well as energy to separate the contributions from different radionuclides [60].

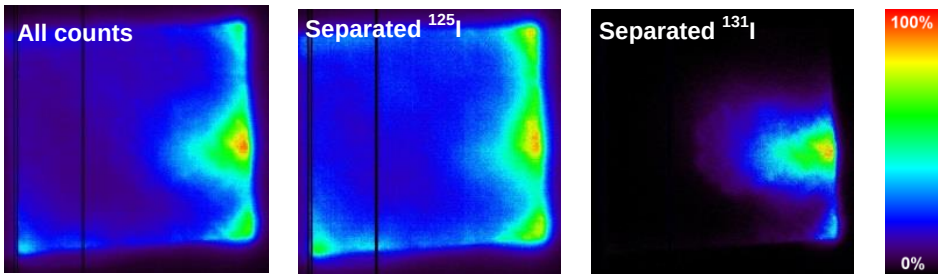

Figure 10.
Autoradiography images from a DSSD system of a piece of filter paper dipped in ^{125}I solution and allowed to dry, after which a drop of ^{131}I solution was applied near one edge: the original image is shown on the left, and the separated contributions from ^{125}I and ^{131}I are shown in the center and on the right. No corrections were applied for faulty strips.

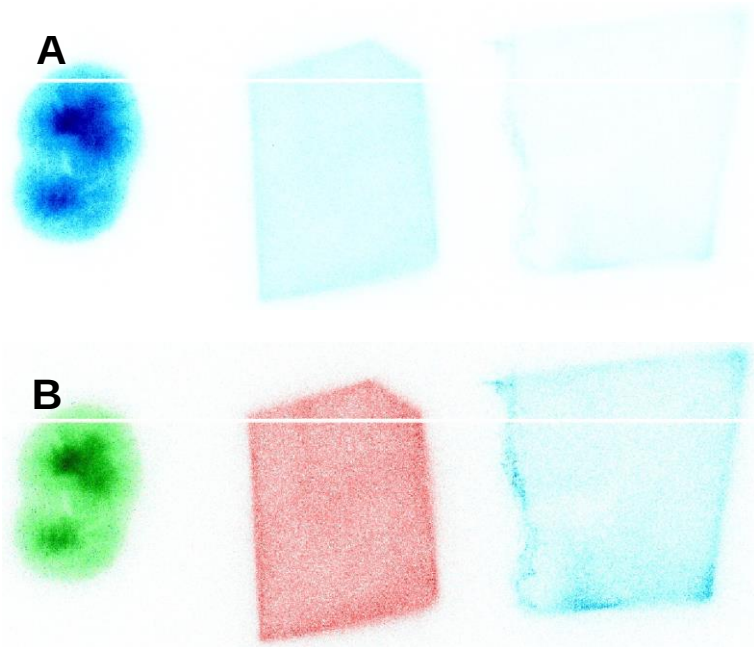

Figure 11.
(A) The total image of three pure radionuclide samples, on a white to blue scale. (B) The separated images showing ^{177}Lu on a white to green scale, ^{18}F on a white to red scale, and ^{99m}Tc on a white to blue scale. No corrections were applied for faulty strips. (Adapted from a poster presentation by Örbom et al. at the World Molecular Imaging Congress 2010.)

Applications

All activities involving live animals described in this thesis were conducted in compliance with Swedish legislation on animal protection, and were approved by the Regional Ethics Committee for Animal Experiments, except in the work described in Paper I, where one study involving animals was performed according to protocols approved by the UCLA Animal Research Committee.

Cancer imaging and therapy using immunoconjugates

Since their introduction in 1975, monoclonal antibodies have been recognized as an excellent tool for diagnosis and treatment of disease because of their high affinity and specificity towards specific antigens [61, 62]. In the case of cancer imaging and therapy, the targeted antigen should show elevated expression on the surface of cancer cells or on cells in the cancer microenvironment, such as in the tumor vasculature. When used for imaging purposes monoclonal antibodies can not only aid in locating tumor cells, but also reveal whether the specific antigen is expressed and available for therapy [61, 63]. Initial antibody development was hampered by the immune response in humans to murine antibodies, but this was remedied by the introduction of chimeric and fully humanized antibodies [61]. Antibodies can have immune-mediated therapeutic effects *per se*, or carry a cytotoxic payload. The work described in this this thesis focuses on imaging and therapy using radioactive labels [62, 64, 65].

A drawback of using full-sized antibodies that have a molecular weight of around 150 kDa is their slow clearance from the blood; they may remain in the circulation for 1-3 weeks. This is not optimal for radiotherapy due to the increased absorbed dose to risk organs such as the bone marrow, and is not ideal for imaging since the background activity will remain high [62, 63]. In addition, it is not easy for large molecules to penetrate bulk tumors, and this is one of the reasons why radioimmunotherapy has so far only been clinically successful in the treatment of disseminated radiosensitive tumors, such as lymphoma [61, 62]. Smaller, engineered antibody fragments (Figure 12) such as diabodies (55 kDa) and minibodies (80 kDa) have been developed, which exhibit faster uptake and clearance more suited for imaging, although tumor uptake is somewhat lower [63]. Affibody molecules (7 kDa), a form of targeting protein scaffolds, exhibit both fast pharmacokinetics and high tumor uptake [66]. These

molecules, as well as peptides used for imaging and therapy [67], are smaller than the glomerular filtration threshold of 60-70 kDa, and will therefore be cleared mostly through the kidneys and not via the liver, which could mean a risk of renal radiotoxicity, especially in therapeutic applications [62, 63].

Another strategy for improving tumor uptake and reducing the absorbed dose from slow-clearing activity is pretargeting, where the antibody is labeled with a molecule, commonly streptavidin, which is easily targeted by another, smaller molecule, commonly biotin, which carries the radionuclide. This allows the physician to wait for optimal antibody distribution before administering the activity, and some promising results have been reported in preclinical and clinical trials [61, 62]. The radionuclide used for labeling is commonly chosen based on the labeling chemistry available and the pharmacokinetics of the molecule. For tracers with rapid clearance, radionuclides with short half-lives are used for imaging (^{18}F, ^{99m}Tc), while for intact antibodies and other molecules with slower uptake and clearance, longer-lived radionuclides (^{89}Zr, ^{124}I, ^{111}In) must be used. In the case of therapy the situation is less clear cut; some longer-lived radionuclides (^{177}Lu, ^{90}Y, ^{131}I) are also being used for smaller molecules.

It can be argued that, barring a major breakthrough, large solid tumors will not be a suitable target for radioimmunotherapy [61], and recent research has been focused on targeting micrometastases and residual disease. Notable strategies include intraperitoneal injections, which lowers the absorbed dose to the bone marrow while still treating possible disseminated disease [68].

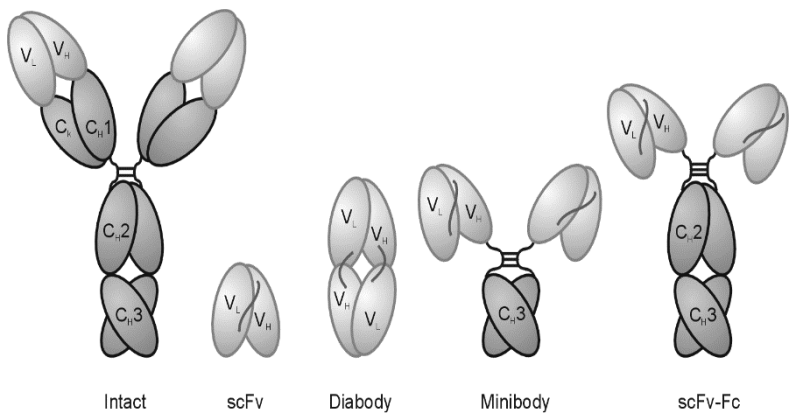

Figure 12.
Intact antibody (150 kDa) and engineered antibody fragments, including single-chain Fv (27 kDa), diabody (50 kDa), minibody (80 kDa), scFv-Fc (105 kDA). (Image provided by Prof. A. Wu, Department of Molecular and Medical Pharmacology, David Geffen School of Medicine at UCLA, Los Angeles, CA, USA.)

Intratumoral distribution of radiolabelled molecules

A factor that affects both imaging and the treatment of primarily solid tumors is the difficulty of macromolecules such as antibodies to penetrate into the tumor and find the targeted antigen. The tumor vasculature is often structurally disorganized, with large distances between vessels and gaps between the inter-endothelial junctions which lower blood flow and increase permeability. At the same time, the function of the lymphatic drainage system is often impaired, elevating the interstitial fluid pressure, impeding tracer penetration [69, 70]. The composition of the extracellular matrix can also limit penetration. Studies have shown that stiffer tumors with a larger amount of collagen are more difficult to penetrate [71, 72]. The density of viable tumor cells also affects the distribution of antibodies, with areas of tightly packed tumor cells, especially common in xenograft animal models, preventing larger molecules from penetrating tight cellular junctions [73-75].

The characteristics of the targeting molecule also affect the intratumoral distribution, with high-affinity antibodies risking capture at a "binding site barrier" where they first encounter the targeted antigen. [76]. Molecular size also determines the speed of diffusion, with smaller antibody fragments penetrating the tumor faster [77]. If the radionuclide label is not residualizing, then that too may lead to a loss of energy imparted to the targeted cell if the antibody is internalized [62].

Some of these effects were investigated using digital autoradiography of the intratumoral activity distribution, and are described in Papers I-V.

Antibodies and diabodies targeting carcinoembryonic antigen (CEA)

The DSSD system and its ability regarding multi-radionuclide imaging was investigated using the intact ^{125}I-labelled anti-CEA chimeric monoclonal antibody T84.66 (cT84.66) [78] and the smaller ^{131}I-labelled engineered fragment T84.66 diabody targeting the same antigen (scFv dimer of 55 kDa) [79] (Paper I). Subcutaneous tumors of the LS174T carcinoma cell line (American Type Culture Collection, Manassas, VA, USA), expressing CEA, were grown on two athymic female mice (nu/nu) (Charles River Laboratories, Wilmington, MA, USA). Once tumors had developed, the mice were given intravenous injections of 12 MBq/101 µg of ^{125}I-cT84.66, and 4 MBq/77 µg of ^{131}I-T84.66 diabody 67 h later. The animals were sacrificed 6 h after the diabody injection.

Tumors were excised, frozen and cryosectioned with alternating section thicknesses of 100 µm and 30 µm. The thicker sections were imaged using the DSSD autoradiography system for 60-840 minutes. The 30 µm thick sections were either stained with hematoxylin and eosin for histological examination, or immunohistochemically stained for the detection of CEA expression. The contributions from ^{125}I and ^{131}I were

separated as described above and in Örbom et al. 2007 [58]). Corrections were made for faulty or miscalibrated detector strips.

The activities of ^{125}I and ^{131}I were both distributed throughout the tumor sections, although an accumulation of ^{125}I was seen in areas of necrotic or interstitial tissue, while hotspots of ^{131}I were observed in areas of viable tumor cells with stronger staining for CEA. Care must be taken not to over-interpret the results of such a small study, especially one using iodine-labeling, which may not be stable once the antibody is internalized [62, 80]. However, the distribution of the intact antibody in more necrotic areas expressing less CEA is in line with the results of previously published studies [80, 81], and the apparent better penetration of the smaller diabody into areas expressing the targeted antigen was also expected [74, 77].

Figure 13 shows the energy-separated images of a kidney from one of the animals studied, which was excised and treated in the same manner as the tumor. The ^{131}I-labelled diabody appears to be concentrated in the cortex, as would be expected for a molecule smaller than the glomerular filtration threshold, while concentration of ^{125}I activity in can be observed in the renal pelvis, probably due to activity in the blood [82].

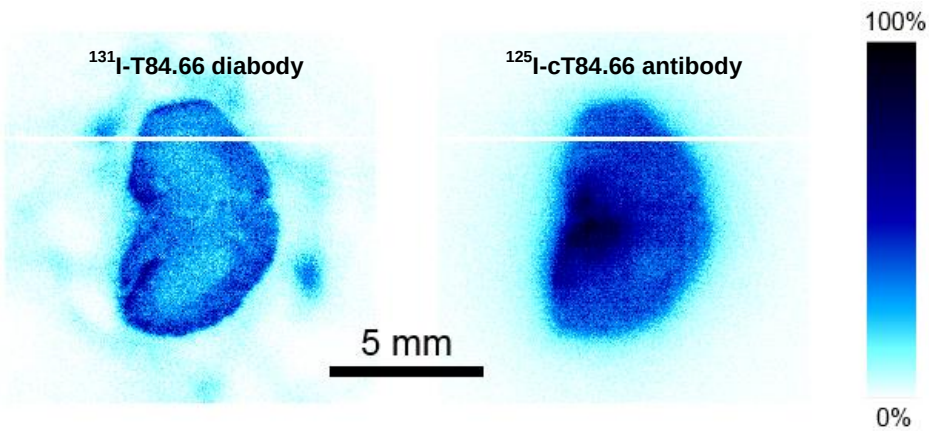

Figure 13.
Multi-radionuclide digital autoradiography images of the distribution of the ^{125}I-labelled monoclonal anti-CEA cT84.66 antibody (150 kDa) in a mouse kidney 73 h after injection, and of the ^{131}I-labelled anti-CEA T84.66 diabody (55 kDa) 6 h after injection. The images were individually scaled from zero to maximum uptake. (Animal model and tracer molecules provided by Anna M. Wu and Tove Olafssen, Department of Molecular and Medical Pharmacology, David Geffen School of Medicine at UCLA, Los Angeles.) No corrections were made for faulty DSSD strips.

Distribution of activity and absorbed-dose rate of ^{177}Lu-DOTA-BR96

The intratumoral distribution of activity after the injection of radiolabeled antibodies was investigated in an animal model for radioimmunotherapy (Papers II and III). In the first of these studies (Paper II), digital autoradiography and immunohistochemical staining were employed to investigate the changes in activity distribution in relation to histology and antigen expression over time at two sub-therapeutic activity levels, while in the second (Paper III), the distribution was imaged in a similar manner, but at therapeutic activity levels, providing complementary information for the comparison of different types of cell death.

The antibody used, BR96 (Seattle Genetics, Bothell, WA, USA), is chimeric, i.e. it has been genetically modified to reduce the risk of an immune response against the antibody in humans [83]. It targets the Lewis-Y (Le^y) antigen, which is expressed on several human cancers such as breast, pancreatic, and gastrointestinal carcinoma, as well as on some normal tissue such as the epithelial tissue of the gastrointestinal tract [84]. It was radiolabelled with ^{177}Lu using a 1,4,7,10-tetraazacyclododecane-1,4,7,10-tetraacetic acid (DOTA) chelate [85]. The dissociation constant (Kd), a measure of the affinity of the immunoconjugate to the antigen, has been determined to be 4 nM [86].

The rat tumor model used was syngeneic, using the BN7005 cell line, originating from colon carcinoma induced in a Brown Norway rat by the carcinogenic compound 1,2-dimethylhydrazine [87], which has been found to have a survival fraction of 55% at a high absorbed dose rate of 2 Gy external irradiation (^{173}Cs) *in vitro*. Immunocompetent male Brown Norway rats (weighing approximately 250 g) were inoculated sub-peritoneally with 3 x 10^5 cells, which were allowed to grow for 13-14 days, reaching a tumor diameter of approximately 1 cm, before injection of the radiolabeled antibody.

Animals were injected intravenously with 150 µg of ^{177}Lu-DOTA-BR96 at the activity levels given in Table 2, where the time of sacrifice is also given for animals not exhibiting complete remission of the tumors. An activity of 400 MBq per kg body weight has previously been shown to result in complete local tumor response in 17 of 19 animals in this model. However, metastases were found in half of the animals [88].

Table 2. Experimental details concerning the animal studies presented in Papers II and III.

Group	Injected activity (MBq/kg)	Number of animals sacrificed at each point in time p.i.									
		2 h	8 h	1 d	2 d	3 d	4 d	5 d	6 d	7 d	8 d
Paper II - 1	50	3	3	2	3	-	3	3	-	-	-
Paper II - 2	25	-	3	3	3	3	3	3	-	3	-
Paper III	400	-	-	3	3	3	3	-	2	-	3

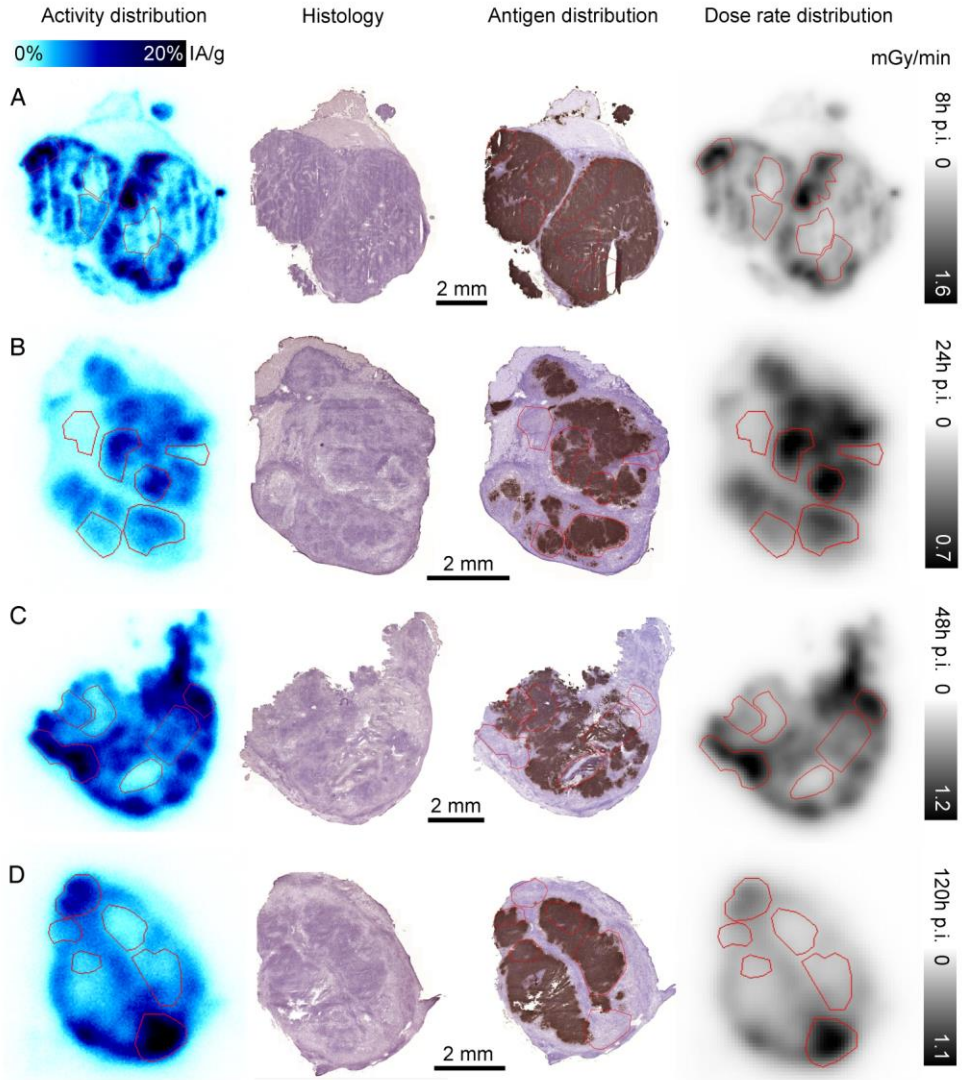

Figure 14.
Representative tumor sections from the study detailed in Paper II at four points in time p.i. From left to right: the digital autoradiography image of ^{177}Lu distribution scaled to %IA/g, followed by adjacent sections stained with hematoxylin and eosin for histological examination, and with BR96 antibody to determine antigen distribution, and finally the absorbed-dose rate distribution at the time of sacrifice based on the activity image (individually scaled). Regions of interest used in correlation analysis are outlined in red where applicable. Note the peripheral distribution of activity in each nodule at 8 h p.i. (A), and the correlation between uptake and antigen at 24 h p.i. (B), which at 48 h p.i. (C) has given way to a correlation between activity and antigen-negative granulation tissue, which is even more pronounced at 120 h p.i. (D). Image and image caption are adapted from Örbom, Eriksson et al 2013 [89].

After sacrifice, the tumors were excised and cut in half. One half was frozen for cryosectioning, and the other was either embedded in paraffin (Paper III), or the activity was measured in a NaI(Tl) well counter (Paper II). Sections 10, 20 or 30 µm in thickness were imaged for at least 10 hours using the DSSD autoradiography system. The images were reconstructed, including corrections for faulty or over-reporting strips, and calibrated to give the percent of injected activity at the time of sacrifice.

Adjacent 10 µm thick cryosections were either stained with hematoxylin and eosin to evaluate histopathology, or immunohistochemically stained for the detection of antigen expression. Staining was performed for the Le^y antigen, for blood vessels (by targeting the anti-endothelial cell antibody RECA-1), and for proliferation (by targeting the protein Ki-67). The paraffin-embedded half was also sectioned, at a thickness of 4 µm, and stained for caspase-3, a marker for apoptosis, γH2AX, a marker for DNA double strand breaks, and for general cell death using the TUNEL assay (Paper III).

At 2 and 8 h post-injection, the activity was mainly found in the tumor margins, which also contained Le^y-positive and viable cells (Figure 14). Tumors had a high proportion of proliferative cells and were overall well vascularized, although staining cannot determine which vessels are functional. At 24 h post-injection, the distribution of activity differed depending on the level of injected activity. Whereas in the first two groups (Paper II) the activity had partially penetrated into areas of viable, Le^y-positive cells, the sections from animals injected with a therapeutic activity (Paper III) exhibited a generally lower cell density, infiltration of stromal tissue and a more varied degree of Le^y expression in areas with relatively high activity uptake (Figure 15). From 48 h post-injection and onwards the sub-therapeutic groups exhibited similar distributions, with activity hotspots increasingly associated with areas of granulation tissue, low Le^y expression and less proliferating cells. This negative association of activity and antigen expression was increasingly evident in all groups at later times. The tumor sizes were measured up until the time of sacrifice and in cases where the size of the tumor decreased, primarily as a result of administration of the therapeutic dose, the activity was found to be more homogeneously distributed in granulation and fibrous tissue that dominated the remaining tumor tissue, with very few proliferating cells. For tumors that increased in size, however, areas of presumably newly grown viable and Le^y-expressing tumor cells were observed, which also stained positive for proliferation, and had very low activity uptake, if any.

The markers for cell death were not directly compared to the activity distribution in Paper III, but it is interesting to note that high levels of γH2AX were detected throughout the whole tumor during the first two days post-injection, but mainly in areas of granulation tissue at later points in time. Caspase-3 staining also showed a similar pattern. In the studies described in both papers, control groups of animals were injected with amounts of unlabeled antibodies comparable to the amounts given to the treated animals, and similar histopathological changes to those seen in the two

groups described in Paper II were observed, i.e., an increase in granulation tissue and a decrease in cell density. This indicates that the observed therapeutic effects at low activity levels were partly due to an immunogenic response mediated via the Fc region of the antibody [64, 65]. Tumors treated with unlabeled antibodies also showed a higher degree of cell death according to the TUNEL assay, but no increase was seen in γH2AX or caspase-3 expression.

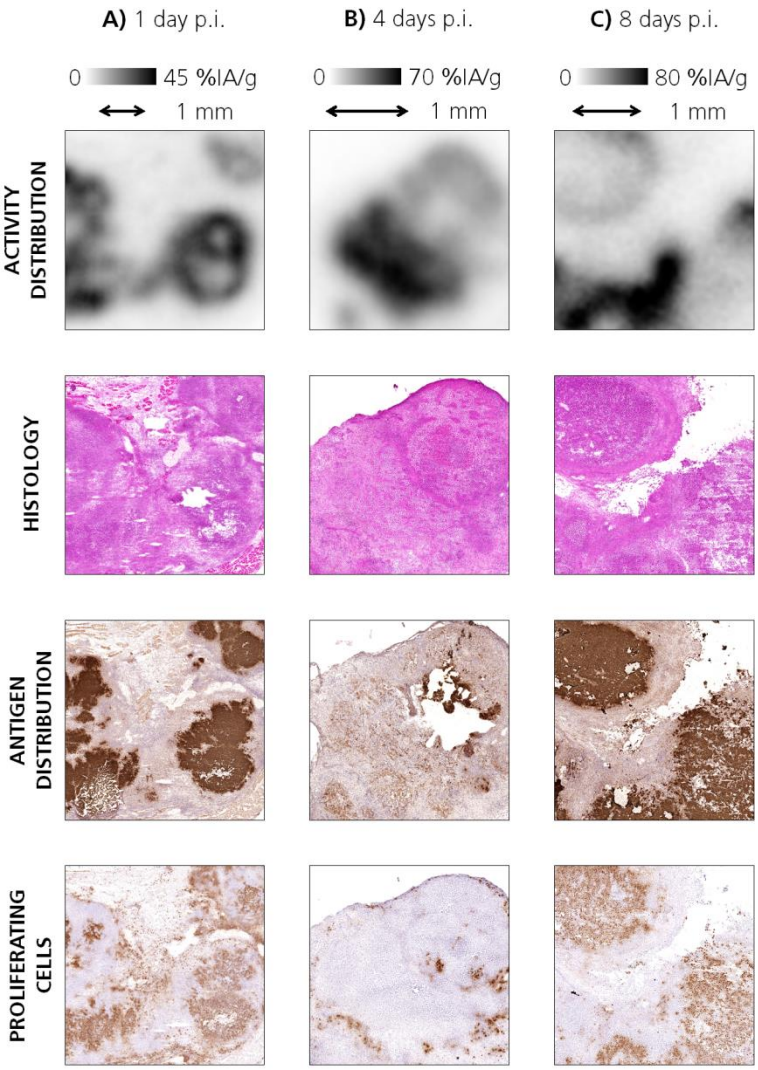

Figure 15. Representative areas of tumor sections 1, 4 and 8 days after the injection of 400 MBq/kg body weight of ^{177}Lu-DOTA-BR96 (Paper III). From top to bottom: Digital autoradiography images of ^{177}Lu distribution, individually scaled to %IA/g, followed by adjacent sections stained with hematoxylin and eosin for histological examination, with BR96 antibody to determine antigen distribution, and finally for the Ki-67 antigen, associated with proliferating cells. Note the elevated levels of activity in areas both with stronger and with weaker levels of Le^{y} expression and correspondingly with both viable tissue and with more granulation tissue at 1 d p.i. (A), and the area of granulation tissue and stromal infiltration and almost no proliferating cells, with a uniform elevated uptake at 4 d p.i. (B), which is again observed at 8 d p.i. (C) in a growing tumor but in this case accompanied by areas of viable tumor cells with very little uptake. (Adapted from a poster by Örbom et al. at the World Molecular Imaging Congress 2012.)

A point-dose kernel for ^{177}Lu, (provided by Erik Larsson, Medical Radiation Physics, Lund University), was used to calculate the absorbed-dose rate distribution in tumor sections at the time of sacrifice. The Monte Carlo code MCNP5 1.4 was used in which the kernel was modeled as concentric spheres of tissue-equivalent medium (1.00 g/cm^3) with radii increasing in steps of 100 μm (Figure 16) [90]. The kernel included all β and γ emissions from ^{177}Lu and was convolved with selected sections stacked to form a three-dimensional volume. It was found that at the resolution of the autoradiography images the absorbed-dose rate closely mirrored the activity distribution, and that areas of high uptake could have twice the absorbed dose rate of the mean over the whole tumor section.

Antibodies targeting ICAM-1 in a prostate cancer mouse model

While improvements have occurred, especially using diffusion weighted magnetic resonance imaging (MRI) and MRI spectroscopy, current imaging methods of prostate cancer still have limited ability to correctly diagnose and stage the disease [91]. ^{18}FDG is unsuited for imaging the often slowly growing tumors near the bladder although other radiolabeled tracers such as ^{18}F- or ^{11}C-Choline or Acetate have shown promise in clinical and preclinical studies [92].

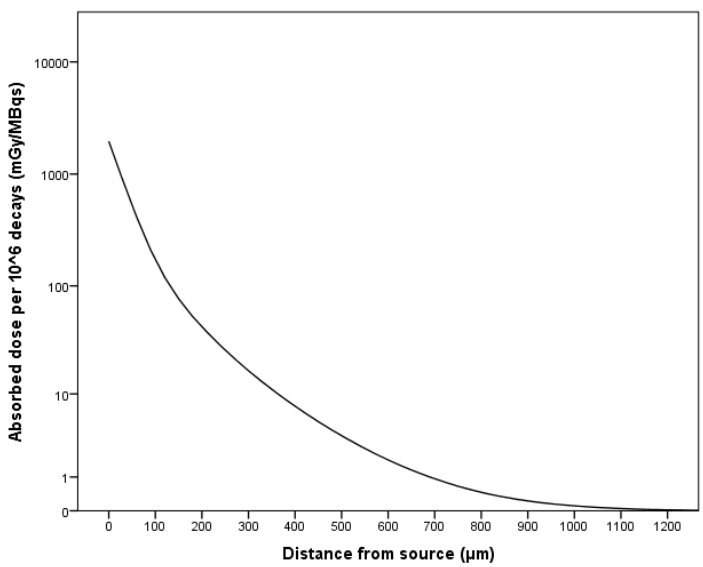

Figure 16.
Profile of a point-dose kernel for ^{177}Lu in a tissue-equivalent medium (1.00 g/cm^3) generated using the Monte Carlo code MCNP5 1.4 (Erik Larsson, Medical Radiation Physics, Lund University).

An antibody targeting the intracellular domain of prostate-specific membrane antigen has been in clinical use for imaging but found limited success due to e.g. accumulation in necrotic areas [93], and the need for improved targeting agents for imaging and therapy remains.

Intercellular Adhesion Molecule 1 (ICAM-1) is a cell surface protein involved in the pathogenesis of prostate cancer. It has been shown that ICAM-1 expression is increased in androgen-insensitive cell lines than in androgen-sensitive ones [94]. R6.5 is a murine IgG_2 monoclonal antibody specific to an extracellular domain of the ICAM-1 molecule [95].

In a study described in Paper IV, radiolabeled R6.5 was evaluated for its targeting potential and biodistribution properties in a mouse subcutaneous xenograft model of human prostate cancer, using small animal SPECT/CT, *ex vivo* multi-radionuclide digital autoradiography, immunohistochemistry and biodistribution. Comparisons were also done with small animal PET/CT of animals injected with both ^{177}Lu-R6.5 mAb and either ^{18}FDG or ^{18}F-Flourocholine (^{18}FCH).

Two separate studies were performed, the first with 9 animals (male NMRI nude mice inoculated with PC-3 tumor cells) with a tumor median size of 81 mm^3 given 4-10 MBq/24-60 µg ^{111}In-labelled R6.5 intravenously. The second with 10 animals given 13-15 MBq/42-48 µg ^{177}Lu-labelled R6.5 and 10 given 14-16 MBq/45-51 µg ^{177}Lu-labelled unspecific IgG2, the combined group of mice having a median tumor size of 986 mm^3. Roughly half of the animals were imaged daily until sacrifice for biodistribution at 48, 72 or 96 hours post-injection using SPECT/CT.

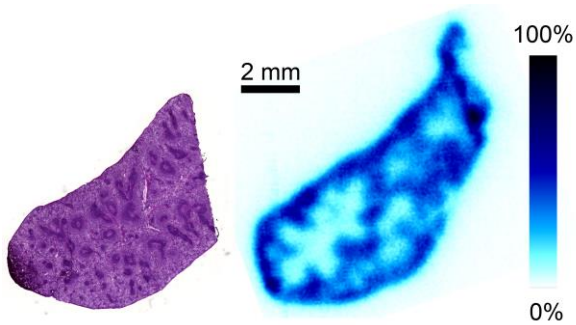

Figure 17.
Hematoxylin and eosin staining and digital autoradiography image of adjacent sections of a (half) spleen from a male NMRI nude mouse inoculated with PC-3 tumor cells, 48 h post-injection of ^{111}In-labelled R6.5 antibody targeting ICAM-1.

The resulting images and the biodistribution data show that while tumor uptake of R6.5 is clearly visible in all animals and is higher (at most 6.07 %IA/g for ^{111}In-R6.5 at 72 h post-injection) than the control antibody, the only statistically significant differences could be found only between ^{177}Lu-IgG2 and ^{111}In-R6.5. This may be due to an observed effect of tumor size where the specific uptake and penetration of R6.5 was worse in larger than smaller tumors. Uptake in the liver was observed, as is expected, but also high uptake in the spleen for all radioimmunoconjugates, especially ^{177}Lu-R6.5 which could possibly be cross-reactivity of the antibody to another target or to mouse ICAM-1. Somewhat surprisingly, PET/CT imaging showed ^{18}FDG better targeting the tumor than ^{18}FCH, but this has been known to be the case in xenograft models as opposed to in patients [92].

For 13 animals, upon sacrifice half of the excised tumor was cryosectioned and digital autoradiography and subsequent staining for histology, vascularization and ICAM-1 expression was performed. For 5 of these tumor section images, radionuclide separation of ^{177}Lu and ^{18}F based on the rate of decay was performed as described earlier in this thesis. The images, as seen in Paper IV, showed ^{111}In-R6.5 and ^{177}Lu-R6.5 accumulating in areas with ICAM-1 expression along the periphery of viable tumor and where viable cells where less densely packed. Elevated levels of uptake could be found where there was strong staining of both the antigen and the vascular marker CD31. The control antibody had a similar distribution, but mainly accumulated in partly necrotic areas and did not correlate as strongly with antigen expression. It is likely that both R6.5 and IgG2 are affected by the barriers to tumor penetration of antibodies discussed earlier. For the single imaged spleen, a very clear pattern was observed with ^{111}In-R6.5 uptake in the red, but not in the white pulp (Figure 17). The activity distribution of ^{18}FDG followed that of viable tumor cells, with elevated levels in the more dense areas inside the tumor while ^{18}FCH accumulated along the edges of viable areas and had low uptake in both necrotic and dense, viable, areas where cells may be under more hypoxic conditions and less proliferative.

The results in Paper IV show that ICAM-1 ha potential as a target for prostate cancer. Further studies must be carried out however, preferably with a chimeric or humanized antibody, to evaluate what dose regimen is optimal for tumor uptake and penetration, as well as if uptake in the spleen can be reduced.

Antibodies targeting free prostate-specific antigen

Prostate-specific antigen (PSA) is abundantly secreted during every clinical stage and grade of prostate cancer. Most of the PSA in blood forms complexes with other molecules, but a smaller fraction remains as free, unbound forms (fPSA). As these are smaller (28 kDa) than the complexes (approx. 90 kDa) they will be rapidly cleared via the kidney, and will not be retained in the blood or liver [96]. Antibodies specifically

targeting fPSA were investigated regarding the feasibility of using them for targeted treatment of prostate cancer (Paper V). A murine antibody, PSA30, was labeled with ^{125}I and 10 MBq/15 µg per animal was injected into 36 male nude mice with subcutaneously implanted tumors grown from LNCaP human prostate cancer cells.

A biodistribution study was performed by sacrificing the animals at 4, 24, 72, 168, and 312 hours, yielding a maximum tumor uptake of 4.32 ± 5.26 %IA/g 24 h post-injection. However, the tumor-to-blood activity ratio peaked at 0.78, and there was a high and increasing uptake of activity in the thyroid, making the evaluation of the overall performance of the antibody difficult. It is suspected that dehalogenation, leading to a high amount of free iodine, influenced the results.

A few of the mice included in this biodistribution study were also given intravenous injections of either the metabolic tracer ^{18}FDG (5 animals, 24, 72, 168, and 312 hours after injection of the antibody) or the cellular proliferation tracer ^{18}FCH (2 animals, 48 hours after injection of the antibody). The animals were sacrificed one hour after these injections, and the tumors excised and cryosectioned at alternating thicknesses of 100 µm and 20 µm; the thicker sections being imaged using the DSSD autoradiography system. The thinner sections were stained either with hematoxylin and eosin for histology, or for the detection of all forms of PSA, using immunohistochemistry. The contributions from ^{125}I and ^{18}F were separated as described above.

It can be seen from the images in Paper V that ^{125}I-PSA30 uptake was generally correlated to staining for PSA-producing LNCaP cells, in particular in the proximity of blood vessels or capillaries. While there was some uptake throughout the denser tumor tissue, elevated ^{125}I activity was also found in more sparsely populated, necrotic areas, without PSA expression. This was probably the effect of either pooling of free iodine or barriers preventing tumor penetration, as discussed above. Neither the activity uptake nor the staining for PSA was correlated with the distribution of either ^{18}FDG or ^{18}FCH. The former was accumulated in viable, possibly inflammatory, areas, and the latter around the tumor edges in well vascularized areas of dense, probably proliferating, cells. These results indicate some degree of specific targeting of the PSA30 antibody *in vivo*. Good targeting has been reported in studies on another fPSA antibody, 5A10, which was labeled using radiometal ^{89}Zr [97].

Imaging of atherosclerotic plaque

Atherosclerosis is a chronic inflammatory disease that develops in response to the accumulation of oxidized lipids and lipoproteins in the arterial wall [98]. The plaques that develop may progress to the stage where there is a risk of rupture, causing thrombosis with possibly fatal consequences. The imaging techniques currently used

to diagnose and stage atherosclerosis include intravascular ultrasound and optical coherence tomography, which mainly provide a measure of the plaque burden, but do not allow direct assessment of the risk of rupture. Molecular imaging strategies are now being introduced in an attempt to evaluate inflammation or cell death, both of which are elevated in atherosclerosis [99]. The imaging of atherosclerosis using ^{18}FDG is now an active area of preclinical and clinical research, and studies have already shown a correlation between ^{18}FDG uptake and macrophages, but not unreservedly with plaque instability [100].

An Antibody targeting oxidized low-density lipoprotein

A human antibody, 2D03, targeting oxidized low-density lipoprotein (LDL) was evaluated regarding its uptake in atherosclerotic plaque and the aortic wall (Paper VI). Oxidized LDL promotes inflammation in atherosclerosis, and antibodies targeting oxidized LDL have been shown to slow plaque development [101]. A mixture of 2D03 and a non-specific control antibody was injected into 12 apoB-100/LDL receptor-deficient mice with heavily developed atherosclerosis. In the case of 8 mice, the specific antibody was labeled with ^{131}I and the control antibody with ^{125}I; in the remaining 4 mice the labeling was reversed. After 72 hours, the animals were given an injection of ^{18}FDG, and were sacrificed one hour later. The descending aorta was dissected, opened longitudinally, and mounted *en face* on a microscope slide. The aortas were imaged using the DSSD system directly following mounting, for at least 1 hour, and again after ^{18}F decay for at least 8 hours. The activity from the three radionuclides was separated as described above. After imaging, the aortas were stained with Oil Red O, which colors lipids red, allowing areas of plaque to be mapped. The activity distribution images were registered to the mapped aortas using rigid transformations and numerical Powell optimization [59]. The ratio of the mean activity in areas defined as plaque to the mean activity in areas defined as plaque-free aorta wall was calculated for each image, and compared using non-parametric statistical analysis.

The plaque-to-aorta activity contrast was highest for 2D03 and lowest for ^{18}FDG for all radionuclide combinations, but the difference was only statistically significant for the study on the 8 mice in which the specific antibody was labelled with ^{131}I. As can be observed in Figure 18, the distributions of the specific and non-specific antibodies in the aorta were very similar. Although the total uptake of the specific antibody in the aorta was higher and additional immunohistochemical analysis, in which the antibodies were directly stained, indicated greater binding of the specific antibody than the non-specific control antibody. The autoradiography images were noisy due to poor statistics and the resolution was degraded due to low-energy X-rays, emphasizing the importance of choosing appropriate radionuclides and administering them at sufficiently high activities for acceptable image quality. The results of this study indicate that 2D03 may be a suitable tracer for atherosclerotic plaque, but

different radiolabels with more comparable image quality should be employed in future studies to investigate non-specific uptake in plaque. It may also be useful to perform *in vivo* imaging to better determine the pharmacokinetics.

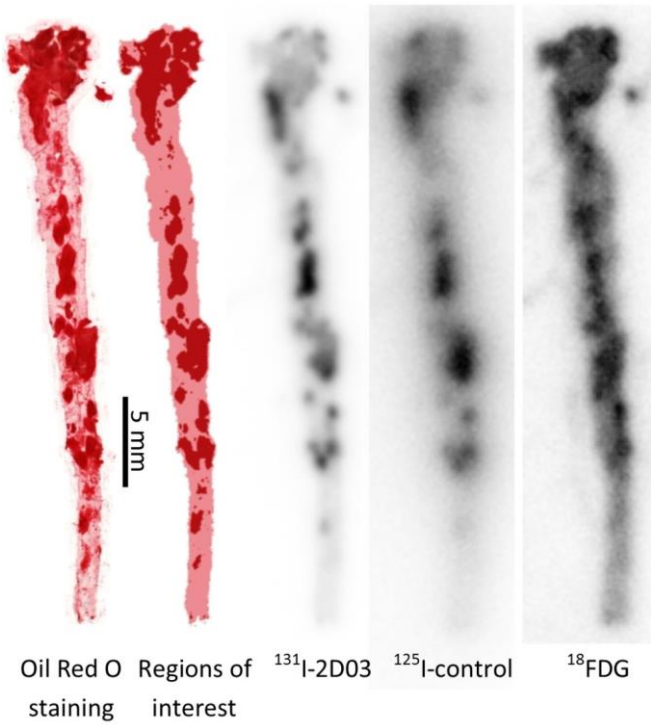

Figure 18.
Images of the aorta from one animal from the study described in Paper VI. From left to right, the aorta was stained with Oil Red O to identify the lipid deposits followed by the processed Oil Red O image to define plaque and non-plaque areas. Finally, with a 5x5-pixel mean filter applied, digital autoradiography images of the same aorta, separated into contributions from the different radiotracers. Each image is individually scaled from zero (white) to max (black) uptake and does not reflect differences in total uptake between different tracers.

Conclusion and future work

A double-sided silicon strip detector system for digital autoradiography has been evaluated regarding its imaging characteristics and its suitability as a complementary imaging modality in preclinical studies using radiolabelled targeting molecules. The instrument was found to perform well with regard to spatial, temporal and energy resolution, compared to the widely used storage phosphor screen technology. However, the field of view is too small for whole-body autoradiography of rodents, and the energy threshold of the detector prohibits imaging of ^{3}H-labeled compounds.

Both single- and multi-radionuclide imaging was performed using the DSSD system in several preclinical studies, yielding useful images of intratumoral and intra-aortic activity distributions, which were quantified in order to display the injected activity per gram, or used for small-scale dosimetry where applicable. Practical difficulties are associated with determining which radionuclides and activity levels are suitable for successful multi-radionuclide digital autoradiography, and careful study design based on data from pilot animal studies will be required to determine these.

Digital autoradiography, especially methods employing modern techniques such as the detector system described in this thesis, has the potential to provide more than illustrative images in preclinical molecular imaging. However, methods of obtaining quantified activity images, as well as absorbed-dose rate distributions, of one or more radionuclides from sample sections must be further developed and validated. The methods developed in this work, together with the data obtained and the experience gained through these studies will aid in that pursuit, but much remains to be done.

Possibilities and limitations of the DSSD system

Imaging of whole-body cryosections of small animals is a major application of autoradiography, especially in drug development [102]. The field of view of the DSSD system is too small for this application, as is the case with many other solid-state autoradiography detectors, although a 13 cm x 13 cm CMOS-based autoradiography detector was recently developed [23]. ^{3}H labeling is also a mainstay in drug development. However, ^{3}H emits β-particles with energies below the detection threshold for this DSSD system [102]. Thus, the most beneficial setting for a detector system of this type is probably in preclinical PET and SPECT studies, using a

number of radionuclides that are detectable by the system and where tissue from individual organs are routinely cryosectioned for staining. The separation of the contributions from different radionuclides could be improved in future work by implementing the recently developed maximum-likelihood algorithm for separation [60]. Whereas most of the imaging studies described in this thesis were carried out at count rates below 400 counts per second, in future studies the system dead time, determined in this work (Paper I) could be utilized to correct for missing counts allowing higher count rates to be used.

The median value calculated from the table of reported spatial resolutions for ^{14}C from published papers on modern digital autoradiography systems compiled by Esposito et al. in 2011 [24] is 36.4 (range 15.3-80) µm, which is much smaller than the 154 µm obtained for ^{58}Co in this work. However, the CSDA range of the electrons of average energy emitted by ^{14}C is only one tenth of that for ^{58}Co, so the resolution of the DSSD system for ^{14}C should be closer to the intrinsic resolution of 50 µm.

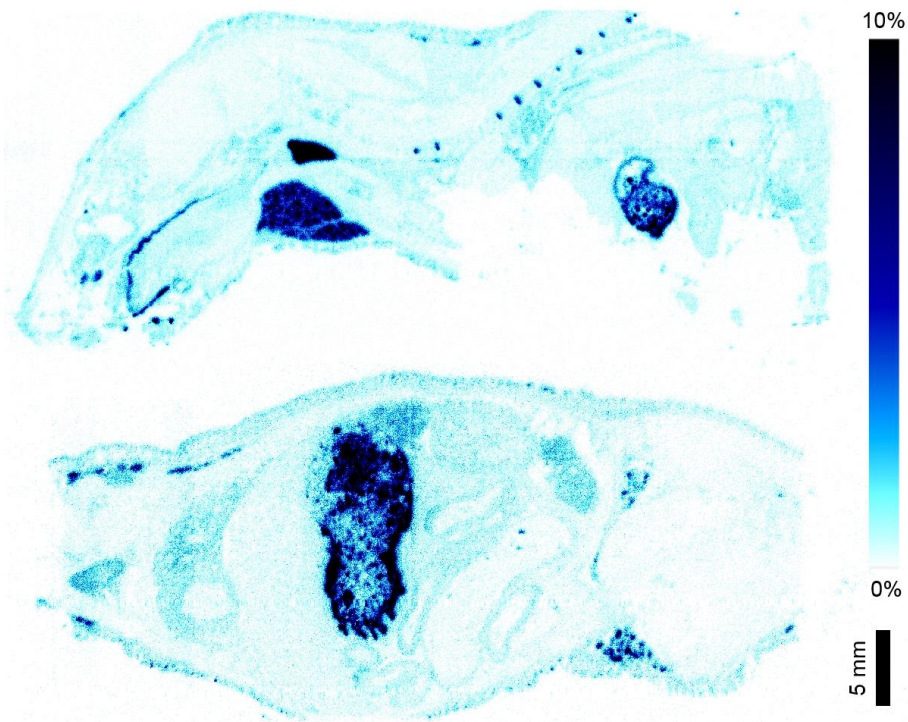

Figure 19.
An image from the DSSD autoradiography system of two half-body sections of normal mice injected with free ^{211}At. (Section courtesy of Tom Bäck, Department of Radiation Physics, Göteborg University. The ^{211}At was produced by Holger J. Jensen, Cyclotron and PET Unit, KF-3982, Rigshospitalet, Copenhagen, Denmark.)

Using the measured profile of the ^{58}Co line source as a point of reference, Monte Carlo simulations could be employed to create approximate point spread functions for different radionuclides, without having to find ways of creating line or point sources. Such point spread functions have been successfully employed for resolution recovery through the deconvolution of images from storage phosphor screen systems [103], and this method could be applied to the DSSD system, especially for imaging of higher-energy β-emitters.

Another method that could be used to improve the spatial resolution of the DSSD system is some form of particle tracking, to determine the origin of a particle that deposits its energy in several pixels, although this would have to be implemented at the system level [24, 104]. The effects of particle range could be avoided by imaging α-emitters, which deposit most of their energy within a single pixel. No systematic evaluation of α-particle imaging using the DSSD system has yet been performed, although a section of a mouse given free ^{211}At has been imaged with the system (Figure 19).

A method of reconstructing high-resolution, three-dimensional activity distributions that could also be convolved with point dose kernels to give absorbed-dose rate distributions was described at IEEE Nuclear Sciences Symposium / Medical Imaging Conference 2007 [58]. This method of serially sectioning a tumor and recombining the imaged sections has previously been successfully used to create absorbed-dose rate volumes of different antibody-radionuclide combinations by, for example, Flynn et al. in 2001 and Roberson et al. in 2003 [105, 106]. This method was not employed in the studies included in this thesis due to deformation and tearing of the tissue resulting from sectioning. The need for a full three-dimensional activity distribution to estimate the absorbed dose distribution has also been questioned [107]. However, a methodology developed by Axente et al. in 2011 of aligning the data from neighboring sections by non-rigid registration of images of a fluorescent blood flow marker from all sections may provide a means of exploiting this method in future studies [108].

Improving drug penetration in tumors

The changes in intratumoral distribuition over time presented in Papers II and III underscore the fact that tumors are dynamic and are affected by treatment, repopulation of tumor cells, and angiogenesis, etc. [73]. The fact that some of the changes in histopathology may be due to an immunological response mediated via the Fc region of the antibodies highlights the benefit of animal models not based on immune-deficient mice with subcutaneous xenografts which, apart from lacking a full immune response, are known to have tumor-host interactions with regard to stroma, vascularization, etc., that are not similar to human cancers [109]. However, it is

difficult to determine whether the comparatively good penetration of antibodies into dense, viable and antigen-expressing areas observed 24 h after injection (Paper II) is due to the tumors being better vascularized than the xenografts described in Papers I, IV and V. Other factors, such as the antibody dose in relation to antigen distribution, and the comparatively low affinity of the BR96 antibody, are also expected to play a role [76, 110].

The fact that no activity was observed in newly formed, viable cell populations at later points in time in the tumors described in Papers II and III indicates that there is a limited time window for efficient therapy, and that radionuclides with shorter half-lives than ^{177}Lu (6.7 d) could be as efficient, although the kinetics may be different in rodents and humans. The results of the small study presented in Paper I indicate that there is a pronounced difference between the intratumoral distribution of small and large tracers, although the results may have been different if residualizing radiolabels had been used. The study presented in Paper IV would have benefited from co-injection of specific and unspecific antibodies for easier comparison as both the specific and non-specific antibodies appear to be distributed in the periphery of the tumor when compared in separate tumors, although the specific antibodies correlated better with staining of the targeted antigen. The design of the study presented in Paper IV included both SPECT/CT and PET/CT imaging of the same animal, in addition to multi-radionuclide autoradiography. This allowed *in vivo* and *ex vivo* imaging of both antibody distribution and tracers for metabolism. Furthermore, image artifacts can be avoided by performing SPECT and PET in the correct order [111]. Studies can thus be designed for the efficient comparison of different tracers employing the multi-radionuclide capabilities of SPECT, although tracer interaction must be considered. With both the novel tracer and the control compound injected into the same animal, stronger statistical results or a reduced number of animals could also be achieved.

A possible avenue for improving tumor penetration of immunoconjugates and the performance of radioimmunotherapy of solid tumors is by altering the tumor micro-environment to allow for better drug penetration. Drugs that degrade collagen or other proteins in the extracellular matrix of the tumor, thereby decreasing its density, have been shown to improve the penetration of macromolecules [112, 113]. The combination of chemotherapy and radioimmunotherapy has also been reported to increase the penetration of antibodies into the tumor and prolong survival in a mouse model [114]. Digital autoradiography in combination with other in vivo and ex vivo imaging modalities could help determine if these combination therapies, which are more complex and may have additional side effects [115], actually improve the absorbed dose delivered to the targeted tumor cells in preclinical models.

References

1. **Nuclear Decay Data in the MIRD Format** [http://www.nndc.bnl.gov/mird/]
2. **About Nuclear Medicine & Molecular Imaging** [http://www.snm.org/index.cfm?PageID=11202]
3. Solon EG, Schweitzer A, Stoeckli M, Prideaux B: **Autoradiography, MALDI-MS, and SIMS-MS imaging in pharmaceutical discovery and development.** *Aaps J* 2010, **12:**11-26.
4. Kagadis GC, Loudos G, Katsanos K, Langer SG, Nikiforidis GC: **In vivo small animal imaging: current status and future prospects.** *Med Phys* 2010, **37:**6421-6442.
5. Robertson R, Germanos MS, Li C, Mitchell GS, Cherry SR, Silva MD: **Optical imaging of Cerenkov light generation from positron-emitting radiotracers.** *Phys Med Biol* 2009, **54:**N355-365.
6. Liu H, Ren G, Miao Z, Zhang X, Tang X, Han P, Gambhir SS, Cheng Z: **Molecular optical imaging with radioactive probes.** *PLoS One* 2010, **5:**e9470.
7. de Kemp RA, Epstein FH, Catana C, Tsui BM, Ritman EL: **Small-animal molecular imaging methods.** *J Nucl Med* 2010, **51 Suppl 1:**18S-32S.
8. Bloomfield PM, Rajeswaran S, Spinks TJ, Hume SP, Myers R, Ashworth S, Clifford KM, Jones WF, Byars LG, Young J, et al.: **The design and physical characteristics of a small animal positron emission tomograph.** *Phys Med Biol* 1995, **40:**1105-1126.
9. Cherry S, Dahlbom M: **PET: Physics, Instrumentation, and Scanners.** In *PET.* Springer New York; 2004: 1-124
10. Pichler BJ, Kolb A, Nagele T, Schlemmer HP: **PET/MRI: paving the way for the next generation of clinical multimodality imaging applications.** *J Nucl Med* 2010, **51:**333-336.
11. Peterson TE, Shokouhi S: **Advances in preclinical SPECT instrumentation.** *J Nucl Med* 2012, **53:**841-844.
12. Barrett H, Hunter WJ: **Detectors for Small-Animal SPECT I.** In *Small-Animal Spect Imaging.* Edited by Kupinski M, Barrett H: Springer US; 2005: 9-48
13. Meikle SR, Kench P, Kassiou M, Banati RB: **Small animal SPECT and its place in the matrix of molecular imaging technologies.** *Phys Med Biol* 2005, **50:**R45-61.
14. Young B, Wheater PR: *Wheater's functional histology : a text and colour atlas.* 5th edn. Philadelphia: Churchill Livingstone Elsevier; 2006.

15. Maunsbach AB, Afzelius BA: *Biomedical electron microscopy : illustrated, methods and interpretations.* San Diego etc.: Academic Press; 1999.

16. Jonsson B, Strand S-E, Emanuelsson H, Larsson B, Howell R, Narra V, Sastry K, Rao D: **Tissue, cellular, and subcellular distribution of indium radionuclides in the rat.** *Biophysical Aspects of Auger Processes Woodbury, NY: American Institute of Physics* 1992**:**249-272.

17. Adelstein S, Green A, Howell R, Humm J, Leichner P, O'Donoghue J, Strand S, Wessels B: **ICRU Report 67:"Absorbed-dose specification in nuclear medicine".** *J ICRU* 2002, **2:**64-65.

18. Attix FH: *Introduction to radiological physics and radiation dosimetry.* New York: Wiley; 1986.

19. Cabello J, Wells K: **The spatial resolution of silicon-based electron detectors in beta-autoradiography.** *Phys Med Biol* 2010, **55:**1677-1699.

20. Johnstrom P, Bird JL, Davenport AP: **Quantitative phosphor imaging autoradiography of radioligands for positron emission tomography.** *Methods Mol Biol* 2012, **897:**205-220.

21. Ljunggren K, Strand SE: **Beta camera for static and dynamic imaging of charged-particle emitting radionuclides in biologic samples.** *J Nucl Med* 1990, **31:**2058-2063.

22. Cabello J, Bailey A, Kitchen I, Prydderch M, Clark A, Turchetta R, Wells K: **Digital autoradiography using room temperature CCD and CMOS imaging technology.** *Phys Med Biol* 2007, **52:**4993-5011.

23. Esposito M, Anaxagoras T, Larner J, Allinson NM, Wells K: **C-14 autoradiography with a novel wafer scale CMOS Active Pixel Sensor.** *J Instrum* 2013, **8.**

24. Esposito M, Mettivier G, Russo P: **C-14 autoradiography with an energy-sensitive silicon pixel detector.** *Phys Med Biol* 2011, **56:**1947-1965.

25. Overdick M, Czermak A, Fischer P, Herzog V, Kjensmo A, Kugelmeier T, Ljunggren K, Nygard E, Pietrzik C, Schwan T, et al: **A "Bioscope" system using double-sided silicon strip detectors and self-triggering read-out chips.** *Nucl Instrum Meth A* 1997, **392:**173-177.

26. Sanghera B, Ott R: **Preliminary studies using silicon strip detectors in digital autoradiography.** *Nuclear Science, IEEE Transactions on* 1993, **40:**992-995.

27. Barthe N, Chatti K, Coulon P, Maitrejean S, Basse-Cathalinat B: **Recent technologic developments on high-resolution beta imaging systems for quantitative autoradiography and double labeling applications.** *Nucl Instrum Meth A* 2004, **527:**41-45.

28. Chen LY, Gobar LS, Knowles NG, Wilson DW, Barrett HH: **Direct Charged-Particle Imaging System Using an Ultra-Thin Phosphor: Physical Characterization and Dynamic Applications.** *Ieee T Nucl Sci* 2009, **56:**2628-2635.

29. Back T, Jacobsson L: **The alpha-camera: a quantitative digital autoradiography technique using a charge-coupled device for ex vivo high-resolution bioimaging of alpha-particles.** *J Nucl Med* 2010, **51:**1616-1623.

30. Lees JE, Fraser GW, Carthew P: **Microchannel plate detectors for C-14 autoradiography.** *Ieee T Nucl Sci* 1998, **45:**1288-1292.

31. Loke KS, Padhy AK, Ng DC, Goh AS, Divgi C: **Dosimetric considerations in radioimmunotherapy and systemic radionuclide therapies: a review.** *World J Nucl Med* 2011, **10:**122-138.

32. Stabin M: **Radiation Dosimetry: Formulations, Models, and Measurements.** In *Basic Sciences of Nuclear Medicine.* Edited by Khalil MM: Springer Berlin Heidelberg; 2011: 129-144

33. Dewaraja YK, Frey EC, Sgouros G, Brill AB, Roberson P, Zanzonico PB, Ljungberg M: **MIRD pamphlet No. 23: quantitative SPECT for patient-specific 3-dimensional dosimetry in internal radionuclide therapy.** *J Nucl Med* 2012, **53:**1310-1325.

34. SOURCE-TARGET SLO: **MIRD Pamphlet No. 17: The Dosimetry of Nonuniform Activity Distributionsā€" Radionuclide S Values at the Voxel Level.** 1999.

35. Larsson E, Strand SE, Ljungberg M, Jonsson BA: **Mouse S-factors based on Monte Carlo simulations in the anatomical realistic Moby phantom for internal dosimetry.** *Cancer Biother Radiopharm* 2007, **22:**438-442.

36. Xie T, Zaidi H: **Assessment of S values in stylized and voxel-based rat models for positron-emitting radionuclides.** *Mol Imaging Biol* 2013, **15:**542-551.

37. Roeske JC, Aydogan B, Bardies M, Humm JL: **Small-scale dosimetry: challenges and future directions.** *Semin Nucl Med* 2008, **38:**367-383.

38. Dewaraja YK, Ljungberg M, Green AJ, Zanzonico PB, Frey EC: **MIRD Pamphlet No. 24: Guidelines for Quantitative 131I SPECT in Dosimetry Applications.** *Journal of Nuclear Medicine* 2013**:**jnumed. 113.122390.

39. Sgouros G, Roeske JC, McDevitt MR, Palm S, Allen BJ, Fisher DR, Brill AB, Song H, Howell RW, Akabani G, et al: **MIRD Pamphlet No. 22 (abridged): radiobiology and dosimetry of alpha-particle emitters for targeted radionuclide therapy.** *J Nucl Med* 2010, **51:**311-328.

40. Green A, Flynn A, Pedley RB, Dearling J, Begent R: **Nonuniform absorbed dose distribution in the kidney: the influence of organ architecture.** *Cancer Biother Radiopharm* 2004, **19:**371-377.

41. Jonsson L, Liu X, Jonsson BA, Ljungberg M, Strand SE: **A dosimetry model for the small intestine incorporating intestinal wall activity and cross-doses.** *J Nucl Med* 2002, **43:**1657-1664.

42. Larsson E, Meerkhan SA, Strand SE, Jonsson BA: **A small-scale anatomic model for testicular radiation dosimetry for radionuclides localized in the human testes.** *J Nucl Med* 2012, **53:**72-81.

43. Knoll GF: *Radiation detection and measurement.* 3rd ed edn. New York: John Wiley & Sons; 2000.

44. Cekaite L, Hovig E, Hauge HH: **Double-sided silicon strip detectors: new applications within genomics and proteomics.** *Nuclear Instruments and Methods in Physics Research*

Section A: Accelerators, Spectrometers, Detectors and Associated Equipment 2004, **527:**68-72.

45. Berger MJ, Coursey J, Zucker M, Chang J: *Stopping-power and range tables for electrons, protons, and helium ions.* NIST Physics Laboratory; 1998.
46. Lees JE, Murray A, Perkins AC, Fraser GW: **Autoradiography of high-energy radionuclides using a microchannel plate detector.** *Ieee T Nucl Sci* 2002, **49:**153-155.
47. Dooraghi AA, Vu NT, Silverman RW, Farrell R, Shah KS, Wang J, Heath JR, Chatziioannou AF: **Betabox: a beta particle imaging system based on a position sensitive avalanche photodiode.** *Phys Med Biol* 2013, **58:**3739-3753.
48. **ImageJ** [http://imagej.nih.gov/ij/]
49. Cabello J, Bailey A, Kitchen I, Turchetta R, Wells K: **A dual threshold method to independently control spatial resolution and sensitivity in β imaging.** In *Nuclear Science Symposium Conference Record, 2008 NSS'08 IEEE.* IEEE; 2008: 1-7.
50. Honeyman JC: **Nuclear medicine data communications.** *Semin Nucl Med* 1998, **28:**158-164.
51. Petegnief Y, Petiet A, Peker MC, Bonnin F, Meulemans A, Le Guludec D: **Quantitative autoradiography using a radioimager based on a multiwire proportional chamber.** *Phys Med Biol* 1998, **43:**3629.
52. Holschneider DP, Yang J, Sadler TR, Galifianakis NB, Bozorgzadeh MH, Bading JR, Conti PS, Maarek JM: **Changes in regional brain perfusion during functional brain activation: comparison of [(64)Cu]-PTSM with [(14)C]-Iodoantipyrine.** *Brain Res* 2008, **1234:**32-43.
53. Picchio M, Beck R, Haubner R, Seidl S, Machulla HJ, Johnson TD, Wester HJ, Reischl G, Schwaiger M, Piert M: **Intratumoral spatial distribution of hypoxia and angiogenesis assessed by 18F-FAZA and 125I-Gluco-RGD autoradiography.** *J Nucl Med* 2008, **49:**597-605.
54. Iwanishi K, Watabe H, Hayashi T, Miyake Y, Minato K, Iida H: **Influence of residual oxygen-15-labeled carbon monoxide radioactivity on cerebral blood flow and oxygen extraction fraction in a dual-tracer autoradiographic method.** *Ann Nucl Med* 2009, **23:**363-371.
55. Wimber DE, Lamerton L: **Cell population kinetics in the intestine of continuously irradiated mice, using double-labelling autoradiography.** *Radiation research* 1966, **28:**694-700.
56. Johnston R, Pickett S, Barker D: **Double-label image analysis using storage phosphor technology.** *Methods* 1991, **3:**128-134.
57. Kvinnsland Y, Skretting A: **Methods for separation of contributions from two radionuclides in autoradiography with a silicon strip detector.** *Phys Med Biol* 2000, **45:**1183-1193.
58. Orbom A, Dahlbom M, Olafsen T, Wu AM, Strand SE: **Serial digital autoradiography with a silicon strip detector as a high resolution imaging modality for TRT dosimetry.** *Nuclear Science Symposium Conference Record, 2007 NSS '07 IEEE* 2007, **6:**4054-4056.

59. Powell MJ: **A fast algorithm for nonlinearly constrained optimization calculations.** In *Numerical analysis.* Springer; 1978: 144-157

60. Holden M, Glad IK, Hauge HH, Hovig E, Liestøl K: **Image restoration and analysis of biomolecular radioactivity images II.** In *Book Image restoration and analysis of biomolecular radioactivity images II* (Editor ed.^eds.). City: Norwegian Computing Center; 2012.

61. Steiner M, Neri D: **Antibody-radionuclide conjugates for cancer therapy: historical considerations and new trends.** *Clin Cancer Res* 2011, **17:**6406-6416.

62. Wu AM, Senter PD: **Arming antibodies: prospects and challenges for immunoconjugates.** *Nat Biotechnol* 2005, **23:**1137-1146.

63. McCabe KE, Wu AM: **Positive progress in immunoPET--not just a coincidence.** *Cancer Biother Radiopharm* 2010, **25:**253-261.

64. Ferris RL, Jaffee EM, Ferrone S: **Tumor antigen-targeted, monoclonal antibody-based immunotherapy: clinical response, cellular immunity, and immunoescape.** *J Clin Oncol* 2010, **28:**4390-4399.

65. Houot R, Kohrt HE, Marabelle A, Levy R: **Targeting immune effector cells to promote antibody-induced cytotoxicity in cancer immunotherapy.** *Trends Immunol* 2011, **32:**510-516.

66. Tran TA, Rosik D, Abrahmsen L, Sandstrom M, Sjoberg A, Wallberg H, Ahlgren S, Orlova A, Tolmachev V: **Design, synthesis and biological evaluation of a multifunctional HER2-specific Affibody molecule for molecular imaging.** *Eur J Nucl Med Mol Imaging* 2009, **36:**1864-1873.

67. Chen K, Conti PS: **Target-specific delivery of peptide-based probes for PET imaging.** *Adv Drug Deliv Rev* 2010, **62:**1005-1022.

68. Jain M, Gupta S, Kaur S, Ponnusamy MP, Batra SK: **Emerging trends for radioimmunotherapy in solid tumors.** *Cancer Biother Radiopharm* 2013, **28:**639-650.

69. Huang CY, Pourgholami MH, Allen BJ: **Optimizing radioimmunoconjugate delivery in the treatment of solid tumor.** *Cancer treatment reviews* 2012.

70. Jain M, Venkatraman G, Batra SK: **Optimization of radioimmunotherapy of solid tumors: biological impediments and their modulation.** *Clin Cancer Res* 2007, **13:**1374-1382.

71. Netti PA, Berk DA, Swartz MA, Grodzinsky AJ, Jain RK: **Role of extracellular matrix assembly in interstitial transport in solid tumors.** *Cancer Res* 2000, **60:**2497-2503.

72. Choi J, Credit K, Henderson K, Deverkadra R, He Z, Wiig H, Vanpelt H, Flessner MF: **Intraperitoneal immunotherapy for metastatic ovarian carcinoma: Resistance of intratumoral collagen to antibody penetration.** *Clin Cancer Res* 2006, **12:**1906-1912.

73. Jang SH, Wientjes MG, Lu D, Au JL: **Drug delivery and transport to solid tumors.** *Pharm Res* 2003, **20:**1337-1350.

74. Lammers T, Kiessling F, Hennink WE, Storm G: **Drug targeting to tumors: principles, pitfalls and (pre-) clinical progress.** *J Control Release* 2012, **161:**175-187.

75. Minchinton AI, Tannock IF: **Drug penetration in solid tumours.** *Nat Rev Cancer* 2006, **6:**583-592.

76. Rudnick SI, Lou J, Shaller CC, Tang Y, Klein-Szanto AJ, Weiner LM, Marks JD, Adams GP: **Influence of affinity and antigen internalization on the uptake and penetration of Anti-HER2 antibodies in solid tumors.** *Cancer Res* 2011, **71:**2250-2259.

77. Beckman RA, Weiner LM, Davis HM: **Antibody constructs in cancer therapy: protein engineering strategies to improve exposure in solid tumors.** *Cancer* 2007, **109:**170-179.

78. Neumaier M, Shively L, Chen FS, Gaida FJ, Ilgen C, Paxton RJ, Shively JE, Riggs AD: **Cloning of the Genes for T84.66, an Antibody That Has a High Specificity and Affinity for Carcinoembryonic Antigen, and Expression of Chimeric Human Mouse T84.66 Genes in Myeloma and Chinese Hamster Ovary Cells.** *Cancer Res* 1990, **50:**2128-2134.

79. Wu AM, Williams LE, Zieran L, Padma A, Sherman M, Bebb GG, Odom-Maryon T, Wong JYC, Shively JE, Raubitschek AA: **Anti-carcinoembryonic antigen (CEA) diabody for rapid tumor targeting and imaging.** *Tumor Target* 1999, **4:**47-58.

80. Dearling JL, Flynn AA, Qureshi U, Whiting S, Boxer GM, Green A, Begent RH, Pedley RB: **Localization of radiolabeled anti-CEA antibody in subcutaneous and intrahepatic colorectal xenografts: influence of tumor size and location within host organ on antibody uptake.** *Nucl Med Biol* 2009, **36:**883-894.

81. Flynn AA, Boxer GM, Begent RH, Pedley RB: **Relationship between tumour morphology, antigen and antibody distribution measured by fusion of digital phosphor and photographic images.** *Cancer Immunol Immunother* 2001, **50:**77-81.

82. Flynn AA, Pedley RB, Green AJ, Dearling JL, El-Emir E, Boxer GM, Boden R, Begent RH: **The nonuniformity of antibody distribution in the kidney and its influence on dosimetry.** *Radiation research* 2003, **159:**182-189.

83. Yarnold S, Fell HP: **Chimerization of antitumor antibodies via homologous recombination conversion vectors.** *Cancer Res* 1994, **54:**506-512.

84. Hellstrom I, Garrigues HJ, Garrigues U, Hellstrom KE: **Highly tumor-reactive, internalizing, mouse monoclonal antibodies to Le(y)-related cell surface antigens.** *Cancer Res* 1990, **50:**2183-2190.

85. Anderson CJ, Welch MJ: **Radiometal-labeled agents (non-technetium) for diagnostic imaging.** *Chem Rev* 1999, **99:**2219-2234.

86. Eriksson SE, Ohlsson T, Nilsson R, Tennvall J: **Repeated radioimmunotherapy with 177Lu-DOTA-BR96 in a syngeneic rat colon carcinoma model.** *Cancer Biother Radiopharm* 2012, **27:**134-140.

87. Brodin N, Jansson B, Hedlund G, Sjögren H: **Use of a monoclonal rat anti-mouse Ig light chain (RAMOL-1) antibody reduces background binding in immunohistochemical and fluorescent antibody analysis.** *Journal of Histochemistry & Cytochemistry* 1989, **37:**1013-1024.

88. Eriksson SE, Ohlsson T, Nilsson R, Tennvall J: **Treatment with unlabeled mAb BR96 after radioimmunotherapy with 177Lu-DOTA-BR96 in a syngeneic rat colon carcinoma model.** *Cancer Biother Radiopharm* 2012, **27:**175-182.

89. Orbom A, Eriksson SE, Elgstrom E, Ohlsson T, Nilsson R, Tennvall J, Strand SE: **The intratumoral distribution of radiolabeled 177Lu-BR96 monoclonal antibodies changes in relation to tumor histology over time in a syngeneic rat colon carcinoma model.** *J Nucl Med* 2013, **54:**1404-1410.

90. X-5 Monte Carlo Team: **MCNP - A General Monte Carlo N-Particle Transport Code, Version 5, Volume I: Overview and theory, Los Alamos National Laboratory report LA-UR-03-1987.**

91. Lutje S, Boerman OC, van Rij CM, Sedelaar M, Helfrich W, Oyen WJ, Mulders PF: **Prospects in radionuclide imaging of prostate cancer.** *Prostate* 2012, **72:**1262-1272.

92. Jadvar H: **Prostate cancer: PET with 18F-FDG, 18F- or 11C-acetate, and 18F- or 11C-choline.** *J Nucl Med* 2011, **52:**81-89.

93. Osborne JR, Akhtar NH, Vallabhajosula S, Anand A, Deh K, Tagawa ST: **Prostate-specific membrane antigen-based imaging.** *Urol Oncol* 2013, **31:**144-154.

94. Zhao H, Kim Y, Wang P, Lapointe J, Tibshirani R, Pollack JR, Brooks JD: **Genome-wide characterization of gene expression variations and DNA copy number changes in prostate cancer cell lines.** *Prostate* 2005, **63:**187-197.

95. Cosimi AB, Conti D, Delmonico FL, Preffer FI, Wee SL, Rothlein R, Faanes R, Colvin RB: **In vivo effects of monoclonal antibody to ICAM-1 (CD54) in nonhuman primates with renal allografts.** *J Immunol* 1990, **144:**4604-4612.

96. Lilja H, Ulmert D, Vickers AJ: **Prostate-specific antigen and prostate cancer: prediction, detection and monitoring.** *Nat Rev Cancer* 2008, **8:**268-278.

97. Ulmert D, Evans MJ, Holland JP, Rice SL, Wongvipat J, Pettersson K, Abrahamsson PA, Scardino PT, Larson SM, Lilja H, et al: **Imaging androgen receptor signaling with a radiotracer targeting free prostate-specific antigen.** *Cancer Discov* 2012, **2:**320-327.

98. Libby P, Lichtman AH, Hansson GK: **Immune effector mechanisms implicated in atherosclerosis: from mice to humans.** *Immunity* 2013, **38:**1092-1104.

99. Gallino A, Stuber M, Crea F, Falk E, Corti R, Lekakis J, Schwitter J, Camici P, Gaemperli O, Di Valentino M, et al: **"In vivo" imaging of atherosclerosis.** *Atherosclerosis* 2012, **224:**25-36.

100. Kusters DH, Tegtmeier J, Schurgers LJ, Reutelingsperger CP: **Molecular imaging to identify the vulnerable plaque--from basic research to clinical practice.** *Mol Imaging Biol* 2012, **14:**523-533.

101. Schiopu A, Frendeus B, Jansson B, Soderberg I, Ljungcrantz I, Araya Z, Shah PK, Carlsson R, Nilsson J, Fredrikson GN: **Recombinant antibodies to an oxidized low-density lipoprotein epitope induce rapid regression of atherosclerosis in apobec-1(-/-)/low-density lipoprotein receptor(-/-) mice.** *J Am Coll Cardiol* 2007, **50:**2313-2318.

102. Solon EG: **Use of Radioactive Compounds and Autoradiography to Determine Drug Tissue Distribution.** *Chem Res Toxicol* 2012, **25:**543-555.

103. Zhang M, Chen Q, Li XF, O'Donoghue J, Ruan S, Zanzonico P, Ling CC, Humm JL: **Image deconvolution in digital autoradiography: a preliminary study.** *Med Phys* 2008, **35:**522-530.

104. Pratx G, Chen K, Sun C, Axente M, Sasportas L, Carpenter C, Xing L: **High-Resolution Radioluminescence Microscopy of 18F-FDG Uptake by Reconstructing the beta-Ionization Track.** *J Nucl Med* 2013, **54:**1841-1846.

105. Flynn AA, Pedley RB, Green AJ, Boxer GM, Boden R, Begent RH: **Optimizing radioimmunotherapy by matching dose distribution with tumor structure using 3D reconstructions of serial images.** *Cancer Biother Radiopharm* 2001, **16:**391-400.

106. Roberson PL, Yokoyama S, Rogers BE, Buchsbaum DJ: **Three-dimensional dose model for the comparison of 177Lu-HuCC49DeltaCH2 and 177Lu-HuCC49 radioimunotherapy in mice bearing intraperitoneal xenografts.** *Cancer Biother Radiopharm* 2003, **18:**239-247.

107. Lu X, Humm J, Chin L: **Estimate of absorbed dose based on two-dimensional autoradiographic information in internal radionuclide therapy.** *Med Phys* 2001, **28:**328.

108. Axente M, He J, Bass CP, Hirsch JI, Sundaresan G, Zweit J, Pugachev A: **Comprehensive approach to coregistration of autoradiography and microscopy images acquired from a set of sequential tissue sections.** *J Nucl Med* 2011, **52:**1621-1629.

109. Workman P, Aboagye EO, Balkwill F, Balmain A, Bruder G, Chaplin DJ, Double JA, Everitt J, Farningham DA, Glennie MJ, et al: **Guidelines for the welfare and use of animals in cancer research.** *Br J Cancer* 2010, **102:**1555-1577.

110. Rhoden JJ, Wittrup KD: **Dose dependence of intratumoral perivascular distribution of monoclonal antibodies.** *J Pharm Sci* 2012, **101:**860-867.

111. Chapman SE, Diener JM, Sasser TA, Correcher C, Gonzalez AJ, Avermaete TV, Leevy WM: **Dual tracer imaging of SPECT and PET probes in living mice using a sequential protocol.** *Am J Nucl Med Mol Imaging* 2012, **2:**405-414.

112. Choi IK, Strauss R, Richter M, Yun CO, Lieber A: **Strategies to increase drug penetration in solid tumors.** *Front Oncol* 2013, **3:**193.

113. Liu J, Liao S, Diop-Frimpong B, Chen W, Goel S, Naxerova K, Ancukiewicz M, Boucher Y, Jain RK, Xu L: **TGF-beta blockade improves the distribution and efficacy of therapeutics in breast carcinoma by normalizing the tumor stroma.** *Proc Natl Acad Sci U S A* 2012, **109:**16618-16623.

114. Jang BS, Lee SM, Kim HS, Shin IS, Razjouyan F, Wang S, Yao Z, Pastan I, Dreher MR, Paik CH: **Combined-modality radioimmunotherapy: synergistic effect of paclitaxel and additive effect of bevacizumab.** *Nucl Med Biol* 2012, **39:**472-483.

115. Junttila MR, de Sauvage FJ: **Influence of tumour micro-environment heterogeneity on therapeutic response.** *Nature* 2013, **501:**346-354.

Printed by Media-Tryck, Lund University, Sweden

Department of Medical Radiation Physics
Faculty of Science
Lund University

ISBN 978-91-7473-778-3